materials

MDPI

Article

Synthesis, Performance Measurement of $Bi_2SmSbO_7/ZnBiYO_4$ Heterojunction Photocatalyst and Photocatalytic Degradation of Direct Orange within Dye Wastewater under Visible Light Irradiation

Jingfei Luan [1,2,*], Bingbing Ma [1], Ye Yao [1], Wenlu Liu [1], Bowen Niu [1], Guangmin Yang [1] and Zhijie Wei [1]

[1] School of Physics, Changchun Normal University, Changchun 130032, China; mbb216216@126.com (B.M.); yaoye1109@mails.jlu.edu.cn (Y.Y.); LWL7200@126.com (W.L.); niubw2021@126.com (B.N.); yangguangmin@ccsfu.edu.cn (G.Y.); weizj2021@126.com (Z.W.)

[2] State Key Laboratory of Pollution Control and Resource Reuse, School of the Environment, Nanjing University, Nanjing 210093, China

* Correspondence: jfluan@nju.edu.cn; Tel.: +86-(0)-199-5193-9498

Abstract: Originally, the new catalyst Bi_2SmSbO_7 was synthesized by the hydrothermal synthesis method or by the solid-phase sintering method at a lofty temperature. A solvothermal method was utilized to prepare a $Bi_2SmSbO_7/ZnBiYO_4$ heterojunction photocatalyst (BZHP). The crystal structure of Bi_2SmSbO_7 belonged to the pyrochlore structure and face-centered cubic crystal system by the space group of *Fd3m*. The cell parameter a was equivalent to 10.835(1) Å (Bi_2SmSbO_7). With $Bi_2SmSbO_7/ZnBiYO_4$ heterojunction (BZH) as the photocatalyst, the removal rate (RR) of direct orange (DO) and the total organic carbon were 99.10% and 96.21% after visible light irradiation of 160 min (VLI-160M). The kinetic constant k toward DO concentration and visible light irradiation time (VLI) with BZH as photocatalyst reached 2.167 min^{-1}. The kinetic constant k, which was concerned with total organic carbon, reached 0.047 min^{-1}. The kinetic curve that came from DO degradation with BZH as a catalyst under VLI conformed to the second-order reaction kinetics. After VLI-160M, the photocatalytic degradation (PD) removal percentage of DO with BZH as the photocatalyst was 1.200 times, 1.268 times or 3.019 times that with Bi_2SmSbO_7 as the photocatalyst, $ZnBiYO_4$ as the photocatalyst or with nitrogen-doped titanium dioxide as the photocatalyst. The photocatalytic activity (PA) was as following: BZH > Bi_2SmSbO_7 > $ZnBiYO_4$ > nitrogen-doped titanium dioxide. After VLI-160M for three cycles of experiments with BZH as the photocatalyst, the RR of DO reached 98.03%, 96.73% and 95.43%, respectively, which meant that BZHP possessed high stability. By using the experiment of adding a trapping agent, the oxidative purifying capability for degradation of direct orange, which was in gradual depressed order, was as following: hydroxyl radical > superoxide anion > holes. Finally, the possible degradation pathway and degradation mechanism of DO were discussed systematically. A new high active heterojunction catalyst BZHP, which could efficiently remove toxic organic pollutants such as DO from dye wastewater after VLI, was obtained. Our research was meant to improve the photocatalytic property of the single photocatalyst.

Keywords: Bi_2SmSbO_7; $Bi_2SmSbO_7/ZnBiYO_4$ heterojunction; direct orange; photocatalytic degradation; visible light irradiation

Citation: Luan, J.; Ma, B.; Yao, Y.; Liu, W.; Niu, B.; Yang, G.; Wei, Z. Synthesis, Performance Measurement of $Bi_2SmSbO_7/ZnBiYO_4$ Heterojunction Photocatalyst and Photocatalytic Degradation of Direct Orange within Dye Wastewater under Visible Light Irradiation. *Materials* **2022**, *15*, 3986. https://doi.org/10.3390/ma15113986

Academic Editor: John T. Kiwi

Received: 31 December 2021
Accepted: 31 May 2022
Published: 3 June 2022

1. Introduction

Due to high chroma, high chemical oxygen demand and complex composition, dye pollutants from the textile and photographic industries are becoming a serious environmental problem [1–6]. Direct orange S ($C_{33}H_{22}N_6Na_2O_9S_2$) was one of the most common pollutants found in wastewater [7,8], it was mainly used for dyeing textiles, leather and paper. Among various dyes, direct orange (DO) dye was very hard to degrade, however,

DO was frequently used as a standard dyestuff pollutant for evaluating the activity of a photocatalyst under UV-light shining [8–14]. Therefore, the effective degradation of direct orange was a problem to be solved.

The conventional processing methods that we used to degrade those dye contaminates were bio-degradation, electrochemistry, adsorption and flocculation-precipitation [15–22]. However, because of the shortcomings and limitations of each method, the conventional methods of treating wastewater cannot achieve the maximum degradation effect [23]. Since 1972, photocatalytic reaction was firstly found, the photocatalysis technology had been booming due to the strong market demand [24], and is widely used in sewage treatment [25,26]. Photocatalysts could produce oxidation groups under light irradiation via absorbing sunlight as the energy source, decompose organic pollutants to generate oxidative free radicals [25–29], and finally effectively remove organic pollutants. Therefore, photocatalysis technology was scientifically attractive because of its high efficiency, energy-saving and pollution-free characteristics [28,29].

Metal oxides [30–41] and metal sulfides [38–45], such as TiO_2 and ZnO, were the most common types of semiconductor photocatalysts. However, the long-term development of TiO_2 in the market will be limited, because of the wide band gap, meaning that TiO_2 can only absorb UV-light (occupying 5% of the solar energy), and for this reason it cannot make reasonable use of optical energy [46]. A report on the Ni-doped $InTaO_4$ (the chemical formula can be summarized as ABO_4) compound in 2001 showed that the ABO_4 compound had great potential for photocatalytic preparation of hydrogen under visible light irradiation (VLI) [47]. Fortunately, in recent years, $A_2B_2O_7$ compounds as photocatalysts [48,49] have also been reported to be able to degrade pollutants in wastewater. In 2011, for the sake of removing the rhodamine B in wastewater, Luan et al. synthesized and used nano-catalysts Y_2InSbO_7 and Y_2GdSbO_7 for the first time, and studied their structure and photocatalytic properties [48]. Luan et al. prepared Cd_2BiSbO_7 and Gd_2YSbO_7 photocatalysts and studied the structure and catalytic performance of a single catalyst. Based on their report, these two catalysts achieved complete removal of rhodamine B, indicating that they were very good visible light-responsive catalysts [49]. As we all know, small improvements in the construction configuration of quasi-conductor catalysts might facilitate the disassociation of photo-generated current carriers, thereby improving photocatalytic activities [50–56]. There are many effective methods [50–63] which could improve the activity of photocatalysts, such as ions doping, the construction of heterojunctions and photosensitization.

Many methods [50–63] have been proven to be effective, such as ion doping methods, the construction of heterojunctions and photosensitization. Among all the methods mentioned above, the design of composite materials was a promising study sphere of photocatalysts. The composite photocatalyst concentrated the role of a single photocatalyst so that the composite system [50–63] had a higher efficiency of light utilization, photocatalytic performance and chemical stability. As we had reported in the previous work [64], Gd_2YbSbO_7 acted as a photocatalyst, crystallized in a pyrochlore-type structure, therefore, changing its structure seemed to be a possible method for realizing the improvement of the PA. According to all the analysis results which were listed above, we could assume that Gd^{3+} in Gd_2YbSbO_7 was replaced by Bi^{3+}, and the replacement of Yb^{3+} by Sm^{3+} might increase the carrier concentration. Consequently, the electrical transportation and photophysical properties showed an obvious change and improvement in the novel Bi_2SmSbO_7 compound, which might possess advanced photocatalytic performance. In addition, the construction of heterojunctions has been proven to be an effective way to enhance the photocatalytic efficiency [65–82]. Sun et al. realized that the degradation of ciprofloxacin on $BiVO_4$-Bi_2WO_6 nano-heterojunction photocatalyst was driven by visible light. In their report, the nanometer heterogenous junction photocatalyst ($BiVO_4$-Bi_2WO_6) exhibited improved photocatalytic degradation (PD) activity for degrading ciprofloxacin under VLI [65]. Yang et al. prepared the g-C_3N_4@BiOCl visible light-responsive photocatalyst with a hollow flower-like structure through a self-assembly strategy. Due to the excellent charge separation ability under VLI, the heterojunction photocatalyst degradation of rhodamine B

exhibited much higher photocatalytic activity (PA) than g-C_3N_4 and BiOCl [66]. Analyzing the above results, it was known that constructing a heterojunction photocatalyst could not only cause an obvious improvement in the reduction-oxidation property of the catalyst [67] but also improve the reactionary activity. Therefore, a $Bi_2SmSbO_7/ZnBiYO_4$ heterogenous junction photocatalyst was also synthesized, and the performance of this heterojunction photocatalyst in DO degradation was worth looking forward to.

In the article, an X-ray diffractometer (XRD), scan electronic microscope-energetic disperse spectrum (SEM-EDS) and X-ray phoelectron spectrometer (XPS) were utilized for analyzing the structural properties of pure phase $ZnBiYO_4$ and single phase Bi_2SmSbO_7. The removal rate (RR) of DO under VLI with pure phase Bi_2SmSbO_7 as a catalyst, $ZnBiYO_4$ as a catalyst, N-doped TiO_2 (N-dT) as a catalyst or with $Bi_2SmSbO_7/ZnBiYO_4$ heterojunction (BZH) as a photocatalyst was detected. Because the energy band width of $ZnBiYO_4$ was 1.953 eV, which was easily lower than the energy of incident visible light under VLI, it was easy to generate photo-generated electrons and photo-generated holes which were separated efficiently and could not easily be recombined. Therefore, $ZnBiYO_4$ was a visible light responsible catalyst with high photocatalytic activity. Meanwhile, the conduction band potential of $ZnBiYO_4$ was -0.682 eV, which was more negative than -0.33 eV, therefore, the photo-generated electrons on the conduction band of $ZnBiYO_4$ were more likely to interact with dissolved oxygen in water to generate superoxide anion. The superoxide anion had a strong oxidizing effect and could directly oxidize direct orange. The valence band (VB) electric potential of Bi_2SmSbO_7 was 2.539 eV, which was more nonnegative than 2.38 eV. Therefore, holes within the VB of Bi_2SmSbO_7 might oxidize hydroxyl and water into hydroxyl radicals for degrading DO in water. Hydroxyl radicals had a strong oxidizing effect; therefore, the pollutant DO in water could be directly and efficiently oxidized by hydroxyl radicals. At the same time, the energy band width of Bi_2SmSbO_7 was 2.42 eV, thus Bi_2SmSbO_7 was also a visible light responsible catalyst with high photocatalytic activity. Both Bi_2SmSbO_7 and $ZnBiYO_4$ could generate photo-generated electrons and photo-generated holes which were not easily recombined under VLI, and had high photocatalytic activity, thus Bi_2SmSbO_7 and $ZnBiYO_4$ could build a perfect heterojunction together. In this study, our purpose was to prepare novel heterojunction catalysts which could remove DO from pharmaceutic wastewater under VLI. For the first time, a new type of $A_2B_2O_7$ compound Bi_2SmSbO_7 nano catalyst was successfully synthetized and the $Bi_2SmSbO_7/ZnBiYO_4$ heterojunction photocatalyst (BZHP) was proposed for removing DO in dye wastewater more efficiently.

2. Result and Discussion

2.1. XRD Analysis

The structural property of Bi_2SmSbO_7 was confirmed by XRD experiment, and the corresponding results, which were obtained by the Materials Studio program based on the Rietveld analysis method, are shown in Figure 1a. According to the refinement results, Bi_2SmSbO_7 was a pure phase, simultaneously, the cell parameter *a* was equivalent to 10.835(1) Å. Based on the truing result, the observed and the calculated intensities showed a highly consistent pattern, which proved that Bi_2SmSbO_7 was a cubical syngony with a space group of *Fd3m*, and in the refinement model, O atoms were included. Table 1 shows the atomic coordinates and structural parameters of Bi_2SmSbO_7. Figure 1b shows the atomic structure of Bi_2SmSbO_7. It could be concluded from Figure 1a that Bi_2SmSbO_7 crystallized into a pyrochlore-type structure. The full profile structure refinement results of Bi_2SmSbO_7 produced unweighted R factors, R_P = 22.09%, and the space group was *Fd3m*.

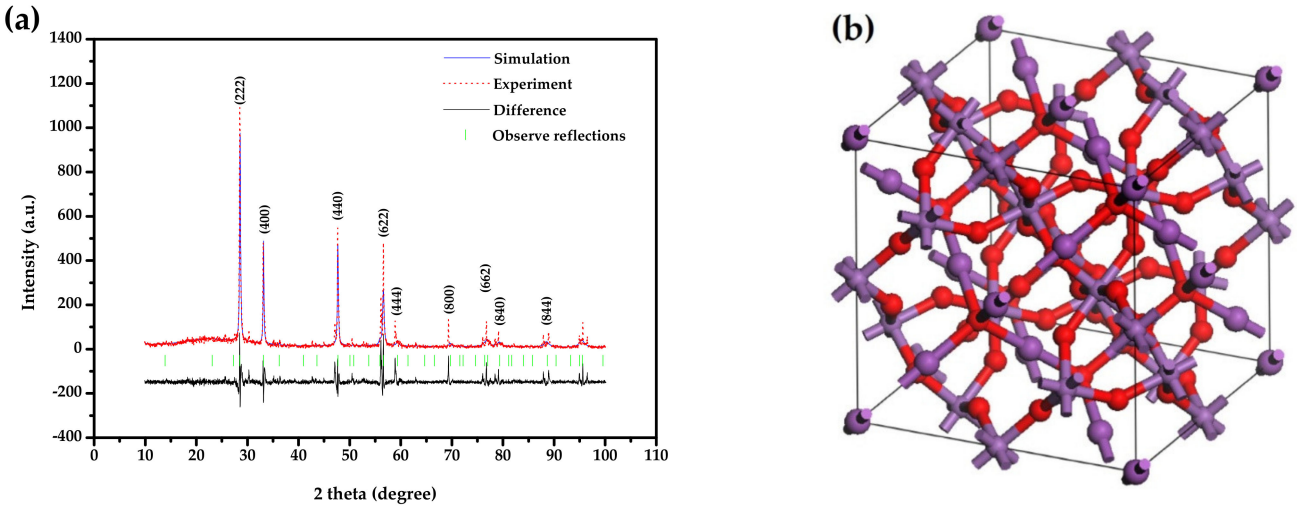

Figure 1. (**a**) XRD and corresponding Rietveld truing of Bi_2SmSbO_7 (red dotted line represents experimentative XRD datum of Bi_2SmSbO_7; blue solid line represents simulative XRD data of Bi_2SmSbO_7; black solid line is the disparity between experimentative XRD datum of Bi_2SmSbO_7 and analogous XRD datum of Bi_2SmSbO_7; green perpendicular is the observed reflective locality); (**b**) Atomy construction of Bi_2SmSbO_7. (Rubious atomy: O, dark purple atomy: Bi, light purpure atomy: Sm or Sb.).

Table 1. Crystallinenature parameters of Bi_2SmSbO_7.

Atomy	x	y	z	Occupation Factor
Bi	0	0	0	1
Sm	0.5	0.5	0.5	0.5
Sb	0.5	0.5	0.5	0.5
O(1)	−0.185	0.125	0.125	1
O(2)	0.125	0.125	0.125	1

It was obvious that the variation sign of the crystalloid structure of the $A_2B_2O_7$ compounds was interrelated with the *x* coordinate of the O (1) atom, when the longness of the A-O (1) bonds was equivalent to the longness of the A-O (2) bonds, and the coordinate was 0.375 [83]. Therefore, if the x value was gained, the information about the distortion of the octahedra (MO_6 (M = Sm^{3+} and Sb^{5+})) could be confirmed [83]. Based on the x value, which was 0.375, the distortion of the MO_6 octahedra could be confirmed to exist in the crystalloid structure of Bi_2SmSbO_7 [83]. For the purpose of preventing recombination of the photoinduced electrons and photoinduced holes, electric charge disjunction was required for PD of direct orange under VLI. According to the reports of Kohno [84] and Nakagawa [85], the localized torsional deformation of the MO_6 octahedron would have helped in inhibiting the electric charge reconfiguration and above-mentioned important factors would, in the end, have contributed to the enhancement of the PA. Based on their theoretical basis, it was easy to conjecture that the torsional deformation of the MO_6 octahedron in the crystalline nature of Bi_2SmSbO_7 could also be considered to be useful for enhancing the PA. Bi_2SmSbO_7 contained a tridimensional network configuration of corner-sharing SmO_6 and SbO_6 octahedrons. Each Bi^{3+} ion was connected to two MO_6 octahedron to form a chain. There were two lengths of Bi-O bonds, three fourths were 2.687 Å (Bi-O (1)) and the rest were 2.273 Å (Bi-O (2)). The six M-O (1) (M = Sm^{3+} and Sb^{5+}) bond lengths were 1.978 Å and the M-Bi (M = Sm^{3+} and Sb^{5+}) bond lengths were 4.353 Å. The M-O-M (M = Sm^{3+} and Sb^{5+}) bond angles were 139.624° in the crystalline nature of Bi_2SmSbO_7. The Bi-M-Bi (M = Sm^{3+} and Sb^{5+}) bond angles were 131.743° in the crystalline nature of Bi_2SmSbO_7. The Bi-M-O (M = Sm^{3+} and Sb^{5+}) bond angles were

135.505° in the crystalline nature of Bi_2SmSbO_7. Many previous reports showed that the luminescent properties were related to the bond angle, which was on the verge of 180°. The locomotivity of the photogenerated electrons and photogenerated holes was enhanced [83] and the PA was improved because the electrons and holes could easily get to the reaction sites of the catalyst surface [83].

Moreover, the Sb–O–Sb bond angle of Bi_2SmSbO_7 was larger, which resulted in an increase in the PA of Bi_2SmSbO_7. In accordance with the above analysis, the effect of degrading direct orange under VLI with Bi_2SmSbO_7 as the catalyst was mainly due to the crystalline nature and electronic crystalline nature.

Figure 2 shows the X-ray diffraction pattern of $ZnBiYO_4$. We have labeled the individual diffractive peaks in Figure 2. The structure of $ZnBiYO_4$ was tested by X-ray diffraction technology. We used the Materials Studio program for analyzing the collected data, and further information about the structure was obtained using the Rietveld analysis method. The conclusion could be made that $ZnBiYO_4$ was single phase and the structure cell parameter of $ZnBiYO_4$ could be equivalent to a = b = 11.176(5) Å and c = 10.014(3) Å. Based on the refinement result, we proved that the crystal formation of $ZnBiYO_4$ went with a quadrigonal spinelle crystalline nature and space group *I41/A*. The band gap of $ZnBiYO_4$ was equivalent to 1.953 eV.

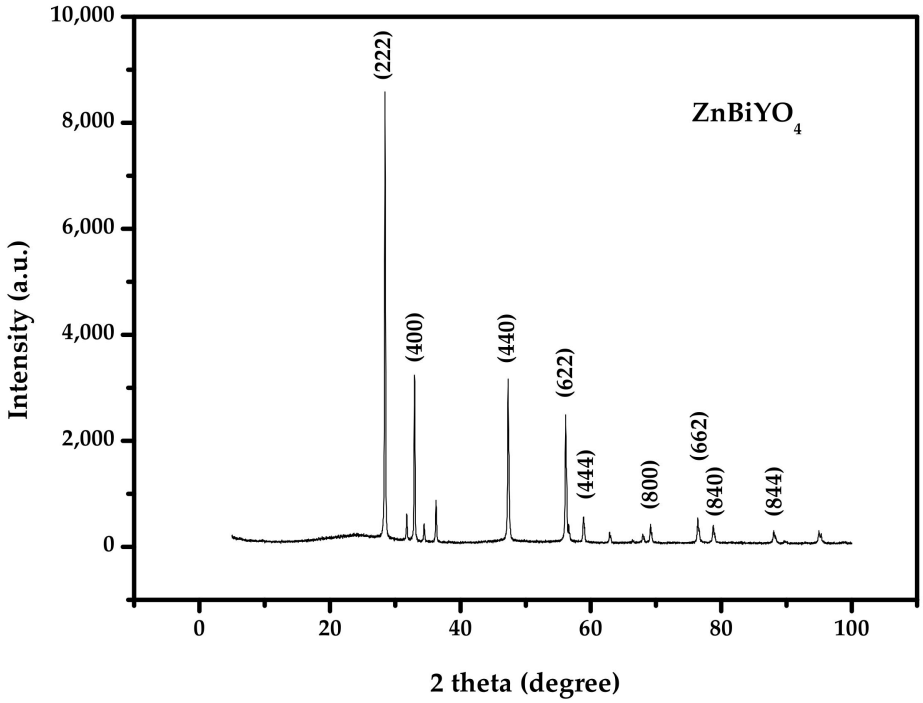

Figure 2. The XRD spectrum of $ZnBiYO_4$.

Figure 3 reveals the XRD spectrum of the $Bi_2SmSbO_7/ZnBiYO_4$ heterojunction photocatalyst. It could be seen from Figure 3 that the pure single-crystal photocatalyst Bi_2SmSbO_7 and single phase photocatalyst $ZnBiYO_4$ existed. Each diffraction peak of Bi_2SmSbO_7 and each diffraction peak of $ZnBiYO_4$ were successfully marked, and other impurities were not found in Figure 3.

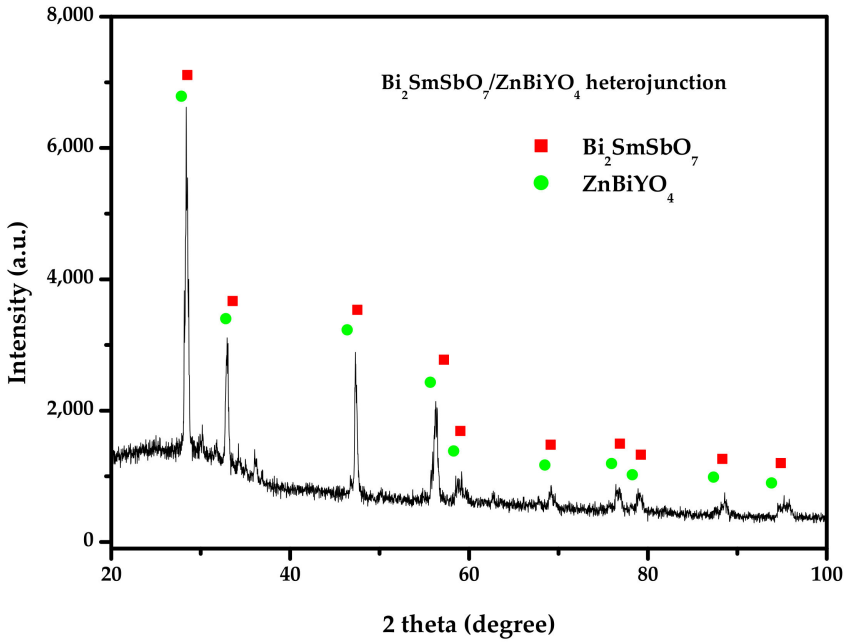

Figure 3. The X-ray diffraction spectrum of $Bi_2SmSbO_7/ZnBiYO_4$ heterojunction.

2.2. Diffused Reflection Spectrum

The absorbing spectra of the Bi_2SmSbO_7 sample are listed in Figure 4a,b. The absorption edge of this new photocatalyst Bi_2SmSbO_7 was at 458 nm which could be found within the seeable light range. The bandgap energy (BGE) of the crystal quasi-conductor was calculated by the Kubelka–Munk function (1) (known as the re-emission function) [86,87].

$$\frac{[1 - R_d(hv)]^2}{2R_d(hv)} = \frac{\alpha(hv)}{S} \quad (1)$$

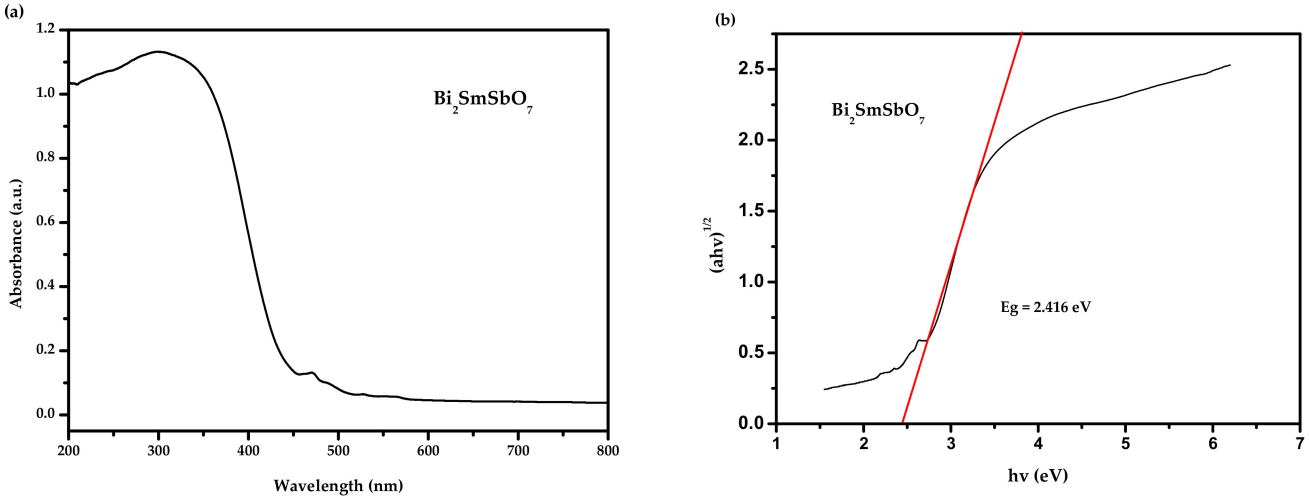

Figure 4. (**a**) The diffused reflection spectrum of Bi_2SmSbO_7; (**b**) Correlative diagram of $(\alpha hv)^{1/2}$ and hv for Bi_2SmSbO_7.

In this function, S represented the scattered factor, R_d represented the diffuse reflectance, and α was absorbance index of radiation.

The absorption which was in the region of the energy band edging of the crystal quasi-conductor followed the equality as (2) [88,89]:

$$\alpha h\nu = A\left(h\nu - E_g\right)^n \quad (2)$$

In this equation, A represents the proportional constant, α represents absorption coefficient, E_g represents band gap and ν represents light frequency, and n determined the transition property of the quasi-conductor.

Following the above procedures, the values of E_g for Bi_2SmSbO_7 could be estimated as 2.42 eV. The estimated merical number of n could be equivalent to about 2, which indirectly allowed the optical transition of Bi_2SmSbO_7.

Figure 5a,b show the UV-Vis diffuse reflectance spectra of $ZnBiYO_4$. According to the above procedures and Figure 5a,b, the merical number of E_g for $ZnBiYO_4$ could be estimated as 1.95 eV. The estimated merical number of n was approximately 2, which indirectly allowed the photic transition of $ZnBiYO_4$.

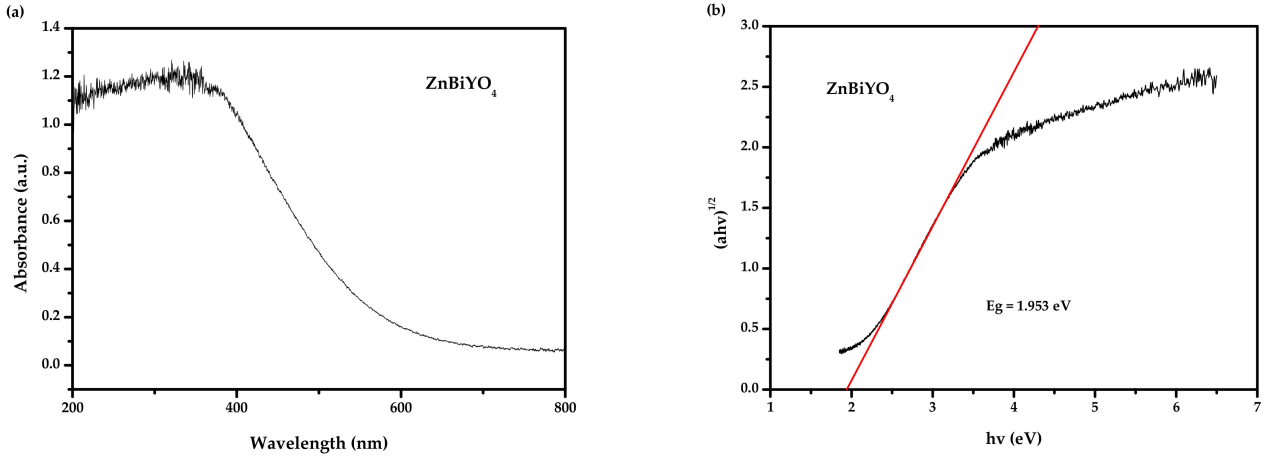

Figure 5. (**a**) The diffused reflection spectrum of $ZnBiYO_4$; (**b**) Correlative diagram of $(\alpha h\nu)^{1/2}$ and $h\nu$ for $ZnBiYO_4$.

Figure 6a,b show the UV-Vis diffuse reflectance spectra of BZH. In accordance with the above procedures and Figure 6a,b, the numerical value of E_g for BZH was calculated to be 2.15 eV. The estimated merical number of n was equivalent to approximately 2, which indirectly allowed the photic transition of BZH.

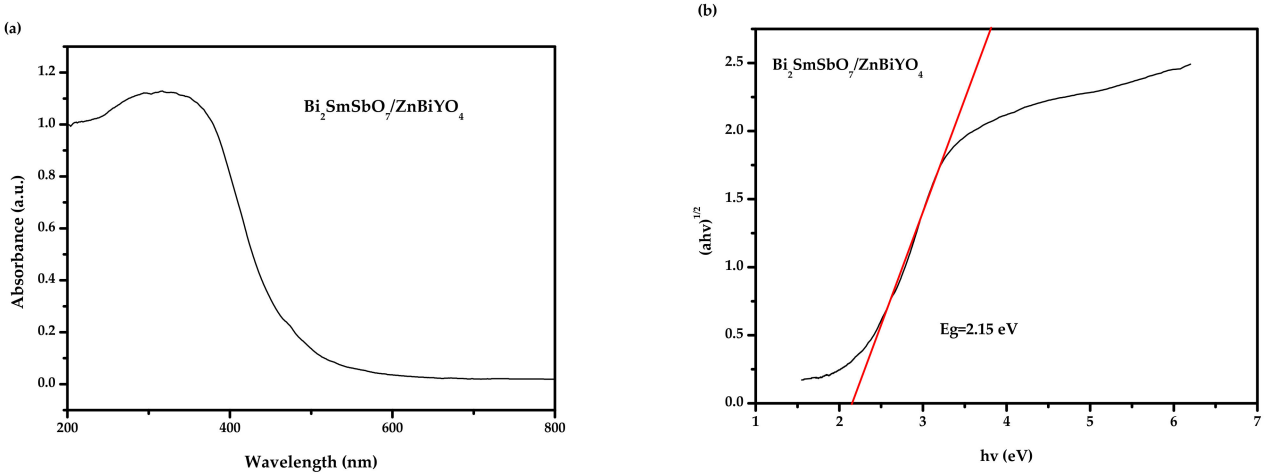

Figure 6. (**a**) The diffused reflection spectrum of $Bi_2SmSbO_7/ZnBiYO_4$ heterojunction; (**b**) Correlative diagram of $(\alpha h\nu)^{1/2}$ and $h\nu$ for $Bi_2SmSbO_7/ZnBiYO_4$ heterojunction.

According to Formula (2), we obtained the following formula $(\alpha h\nu)^{1/2} = h\nu - E_g$, and $(\alpha h\nu)^{1/2}$ was regarded as the y coordinate and $h\nu$ was regarded as the x coordinate. According to Figure 6b, the intersection with the x axis should be the value of E_g = 2.15 eV when y = 0. The BGE of Bi_2SmSbO_7 was 2.42 eV; the BGE of $ZnBiYO_4$ was 1.95 eV; the BGE of BZH was 2.15 eV; the BGE of $Bi_3O_5I_2$ could be equivalent to 2.02 eV [90]; and the BGE of zinc oxide, which was doped with cobalt, could be equivalent to 2.39 eV [91]. Every BGE of the above five compounds was lower than 2.43 eV, meaning that all the compounds would not only show responsive characteristics under VLI, but also possess tremendous potential to exhibit lofty photocatalytic activity.

2.3. Performance Representation of $Bi_2SmSbO_7/ZnBiYO_4$ Heterojunction Photocatalyst

So as to obtain the valence states and the surface chemical compositions of each element of $Bi_2SmSbO_7/ZnBiYO_4$, the XPS was accomplished. Figure 7 shows the XPS comprehensive spectrogram of $Bi_2SmSbO_7/ZnBiYO_4$. Figure 8 represents the XPS spectrogram of O^{2-}, Bi^{3+}, Sm^{3+}, Zn^{2+}, Y^{3+} and Sb^{5+}, which are derived from $Bi_2SmSbO_7/ZnBiYO_4$. Based on the XPS full spectrum, which was shown in Figure 7, the synthesized $Bi_2SmSbO_7/ZnBiYO_4$ included the elements of Bi, Sm, Zn, Y, Sb and O. According to XPS analysis results, which was displayed in Figures 7 and 8, the chemical valence of Bi, Sm, Zn, Bi, Y, Sb or O ion was equivalent to +3, +3, +2, +3, +3, +5 or −2. According to the results of the above analytical tests, the formulae for Bi_2SmSbO_7 and $ZnBiYO_4$ could be determined. It can be seen from Figure 8 that various elemental peaks with specific binding energies were obtained. In Figure 8, the O1s peak of the O element is located at 529.90 eV. The position of the $Bi5d_{3/2}$ and $Bi5d_{5/2}$ peaks were fitted (located at 28.45 eV and 26.05 eV). The position of the $Sm3d_{5/2}$ peak was at 1082.99 eV and the $Sb4d_{3/2}$ peak was located at 35.20 eV. The position of $Zn2p_{1/2}$ or $Zn2p_{3/2}$ peaks were at 1041.72 eV and 1021.45 eV. The position of the $Y3p_{3/2}$ peak of the Y element was at 301.05 eV. In short, Figures 7 and 8 showed the existence of zinc (Zn_{2p}), samarium (Sm_{3d}), antimony (Sb_{4d}), bismuth (Bi_{4f} and Bi_{5d}), Yttrium (Y_{3p}) and oxygen (O_{1s}) within the synthetical catalysts. The results of the superficial element characterization showed that the medial atomistic percentage of Bi:Sm:Sb:Zn:Y:O was equivalent to 940:262:285:384:402:7727. The atomistic proportion of Bi:Sm:Sb or Zn:Bi:Y in the catalyst of BZHP was equivalent to 2.09:1.00:1.09 and 1.00:1.02:1.05, respectively. The reason for the high oxygen value might be owing to the large amount of O which was sorbed on the superficies of $Bi_2SmSbO_7/ZnBiYO_4$. Obviously, it showed that there were no other phases in the XPS peak of $Bi_2SmSbO_7/ZnBiYO_4$ because neither shoulder nor expansion was observed.

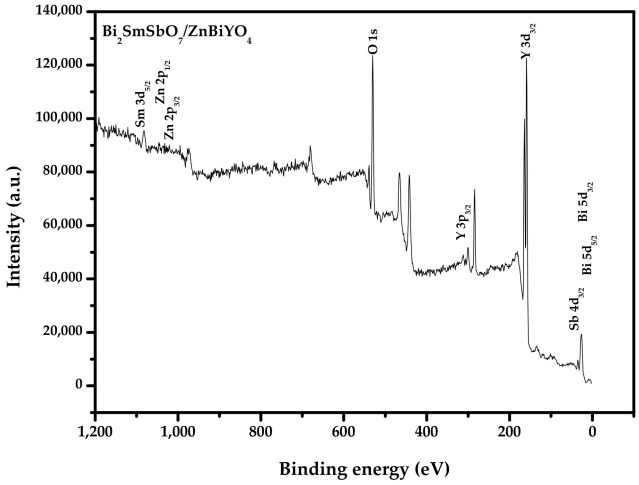

Figure 7. XPS survey spectrum of the $Bi_2SmSbO_7/ZnBiYO_4$ heterojunction photocatalyst.

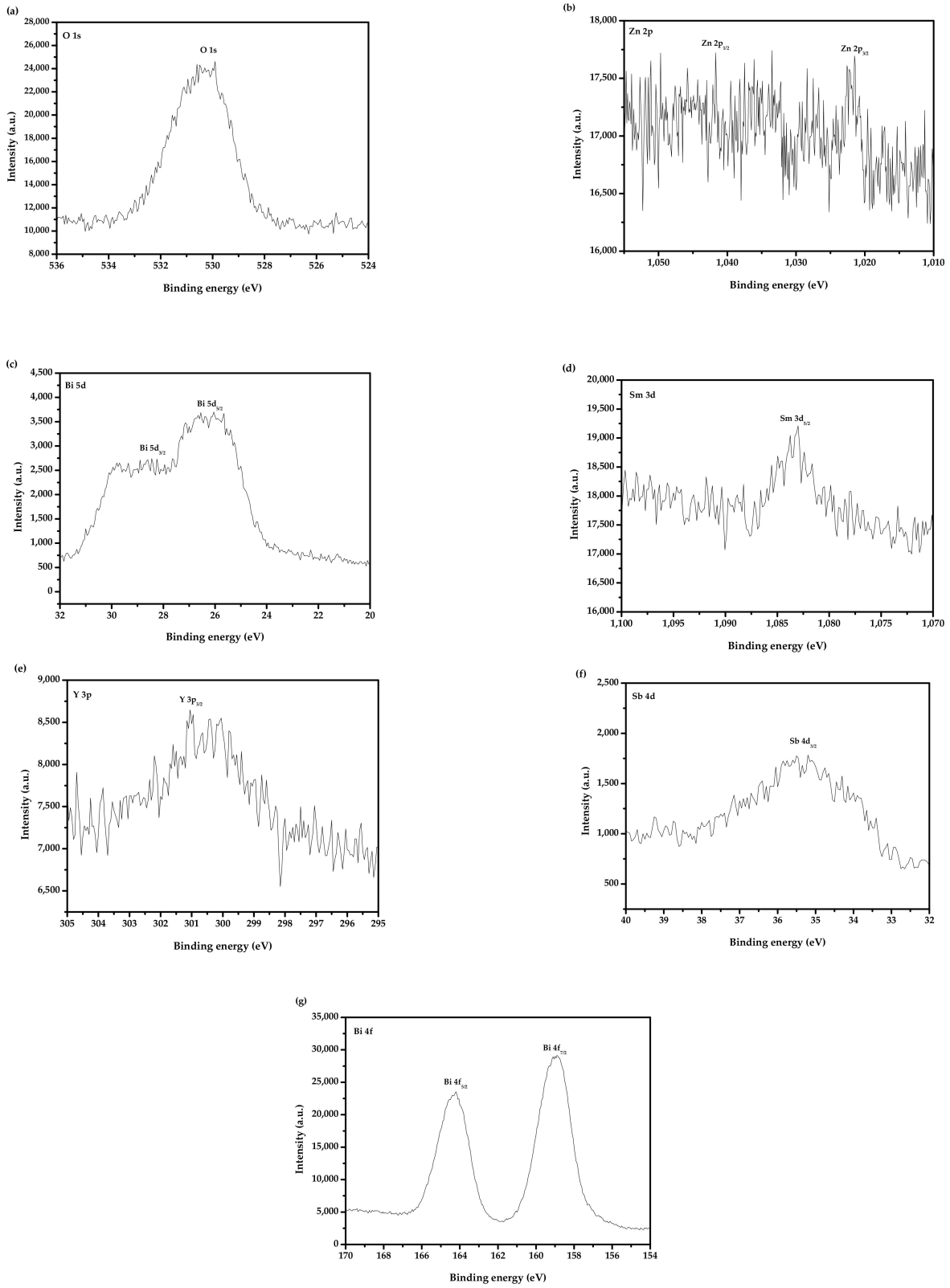

Figure 8. (**a**) XPS of O^{2-} which derived from BZHP; (**b**) XPS of Zn^{2+} which came from BZHP; (**c**) XPS of Bi^{3+} (Bi_{5d}) which came from BZHP; (**d**) XPS of Sm^{3+} which came from BZHP; (**e**) XPS of Y^{3+} which came from BZHP; (**f**) XPS of Sb^{5+} which came from BZHP; (**g**) XPS of Bi^{3+} (Bi_{4f}) which was obtained from BZHP.

Figure 9 shows the SEM image of BZHP. Figure 10 shows the EDS elemental mapping of BZHP. Figure 11 shows the EDS spectra of BZHP. The results of Figure 9 and Figure 10 showed that the large dodecahedron structure belonged to Bi_2SmSbO_7, and the uniformly dispersed spherical flocculent small particles belonged to $ZnBiYO_4$. Small particles of $ZnBiYO_4$ were closely surrounded and loaded on the surface of large particles of Bi_2SmSbO_7. As could be seen from Figures 9 and 10, the particles of Bi_2SmSbO_7 were surrounded by the smaller particles of $ZnBiYO_4$ and all these particles were tightly bound together, which was a strong proof of the successful preparation of BZHP. Bi_2SmSbO_7 possessed a rhombic dodecahedron-like morphology. It was common sense that the distinct surface energy of crystallite facets controlled the structural growth of the photocatalyst. Previously, researchers have discovered that the Ag_3PO_4 (110) surface possessed a higher superficial energy when compared with the (111) surface, therefore, the crystal structure aggregated along the (110) direction, resulting in the formation of a rhombic dodecahedron-like morphology of silver phosphate [92,93]. It could be concluded that the reason why Bi_2SmSbO_7 possessed a diamond-shaped dodecahedron morphology might be illuminated in the above analysis. $ZnBiYO_4$ possessed a regular spherical morphology and a uniform particle distribution (Figure 9). The particle size of Bi_2SmSbO_7 was approximately 2600 nm, while the particle size of $ZnBiYO_4$ was approximately 1000 nm.

The results of the SEM-EDS analysis are shown in Figures 9–11, and other impurities were not found in the BZHP compound. Similarly, the unmingled phase of Bi_2SmSbO_7 had a good agreement with the results of the XRD analysis, which is represented in Figure 1a. From Figures 10 and 11, it can be concluded that BZHP contained bismuth element, samarium element, antimony element, zinc element, yttrium element and oxygen element. The previous results had a good agreement with the XPS results of BZHP. According to the EDS spectrum of BZHP (Figure 11), the atomic ratio of Bi:Sm:Sb:Zn:Y:O was 1213:414:418:405:389:7161, which was also consistent with XPS results of BZHP. The atomic ratio of Bi_2SmSbO_7:$ZnBiYO_4$ was close to 1000:973. Based on the above results, we could conclude that BZHP owned high purity under the preparation conditions which were used in this work.

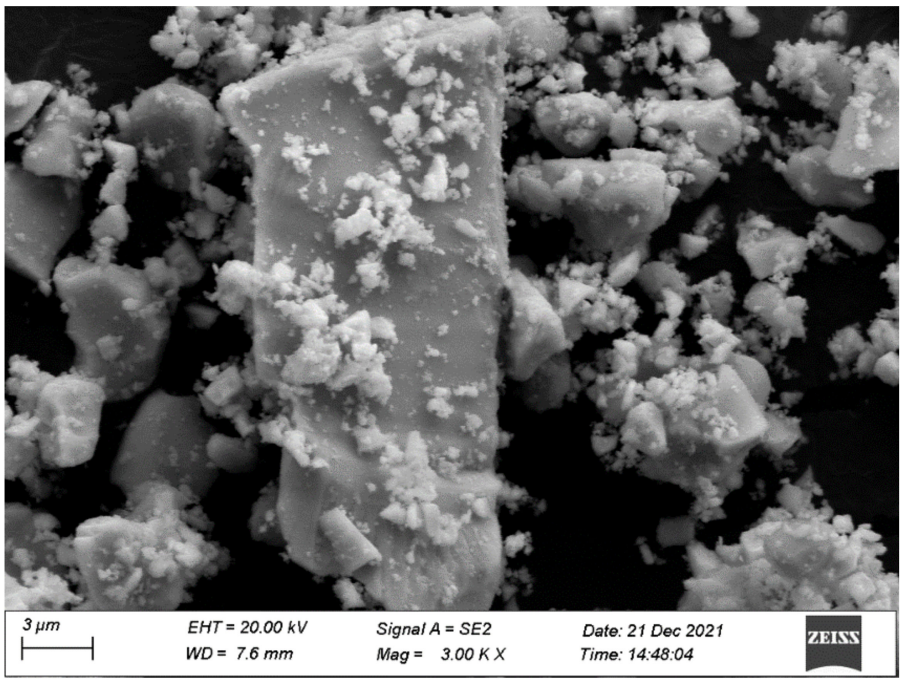

Figure 9. SEM photograph of $Bi_2SmSbO_7/ZnBiYO_4$ heterojunction photocatalyst.

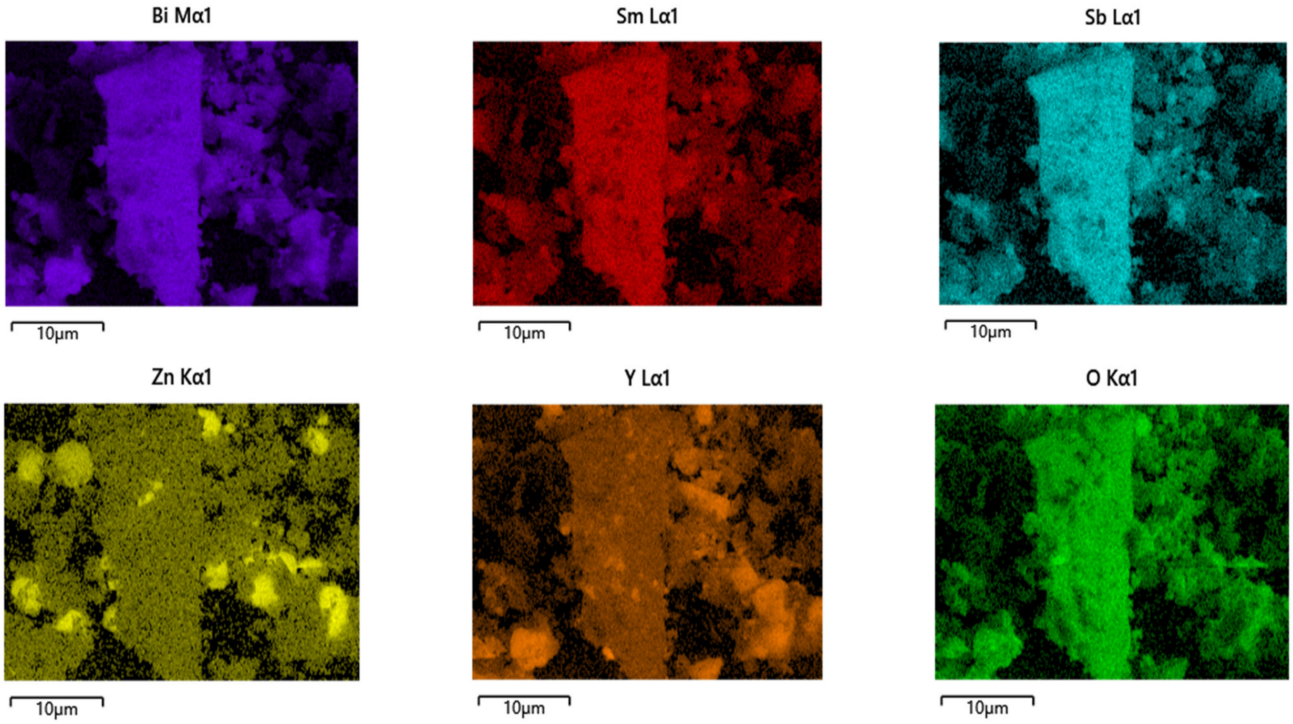

Figure 10. EDS elementary mapping of $Bi_2SmSbO_7/ZnBiYO_4$ heterojunction catalyst (Bi, Sm, Sb, O from Bi_2SmSbO_7 and Zn, Bi, Y, O from $ZnBiYO_4$).

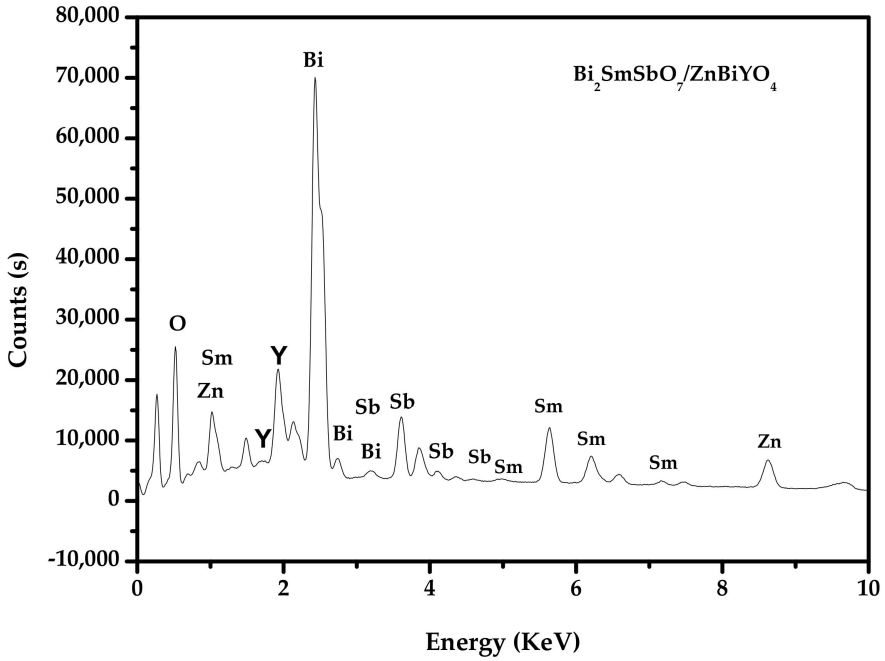

Figure 11. EDS spectrum of $Bi_2SmSbO_7/ZnBiYO_4$ heterojunction photocatalyst.

2.4. Photocatalytic Activity

Figure 12 shows the concentration variance bights of DO during PD of DO with BZH as catalyst or with Bi_2SmSbO_7, $ZnBiYO_4$ and N-dT as catalyst under VLI. It could be found from Figure 12 that the concentration of DO within dye wastewater gradually decreased with increasing visible light irradiation time when $Bi_2SmSbO_7/ZnBiYO_4$ heterojunction or Bi_2SmSbO_7 or $ZnBiYO_4$ or N-dT was utilized as a catalyst for degrading DO. In all the contrast experiments, the VLI time was set to be 160 min. The results which were obtained from

Figure 12 showed that after VLI-160M, with BZH as the catalyst, the RR value of DO in dye wastewater achieved 99.10%, the reactive rate was equivalent to 3.097×10^{-9} mol·L^{-1}·s^{-1}, and the photon efficiency (PE) was equivalent to 0.0651%. With Bi_2SmSbO_7 as the photocatalyst or with $ZnBiYO_4$ as the photocatalyst, the RR decreased. When Bi_2SmSbO_7, $ZnBiYO_4$ or N-dT were utilized as the photocatalyst, the RR of DO achieved 82.57%, 78.13% or 32.83%, the rate of reaction was equivalent to 2.58×10^{-9} mol·L^{-1}·s^{-1}, 2.44×10^{-9} mol·L^{-1}·s^{-1} or 1.03×10^{-9} mol·L^{-1}·s^{-1}, and the PE was equivalent to 0.0542%, 0.0513% or 0.0216%, respectively. Therefore, it was obvious that the photodegradation efficiency of DO was the highest when using BZHP. By calculating the contrast experimental results, the RR of DO by using BZH was 1.200 or 1.268 or 3.019 times higher than that with Bi_2SmSbO_7 as the catalyst, $ZnBiYO_4$ as the catalyst or with N-dT as the catalyst. Using Bi_2SmSbO_7 as the photocatalyst or BZHP as the photocatalyst, respectively, the concentration of nulvalent Sb or Sb^{5+} in the aqueous solution before photocatalytic degradation of direct orange was zero. After VLI-160M for PD of DO, the content of nulvalent Sb or Sb^{5+} in the aqueous solution was also zero. Regarding the specific surface area, the specific surface area of Bi_2SmSbO_7 was 4.15 m^2/g, the specific surface area of $ZnBiYO_4$ was 4.06 m^2/g, and the specific surface area of BZHP was 4.12 m^2/g. All of our photocatalytic reactions (Figure 12) were realized by the photocatalysts which were prepared by the hydrothermal synthesis method; thus, it would not cause a difference in photocatalytic activity.

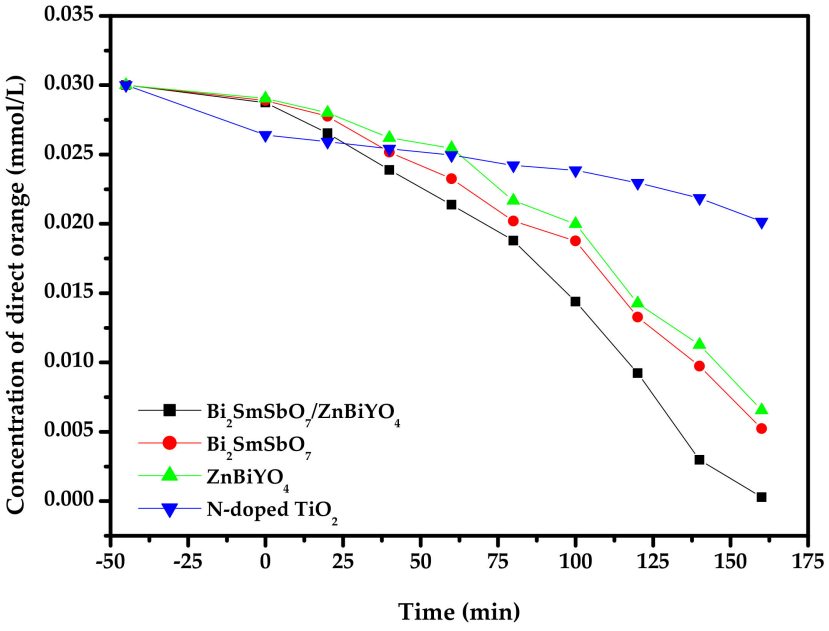

Figure 12. Concentration variation curves of DO during PD of DO with $Bi_2SmSbO_7/ZnBiYO_4$ heterojunction as catalyst or with Bi_2SmSbO_7, $ZnBiYO_4$, N-doped TiO_2 as catalyst under VLI.

Figure 13 shows the concentration changing curved line of total organic carbon (TOC) during PD of DO in dye wastewater with BZH or with Bi_2SmSbO_7 or with $ZnBiYO_4$ or with N-dT as catalyst under VLI. The concentration of DO gradually decreased with increasing VLI time. As could be found from Figure 13, the RR of TOC within dye wastewater reached 96.21%, 73.54%, 68.71% and 25.78%, respectively, after VLI-160M when BZHP, Bi_2SmSbO_7, $ZnBiYO_4$ and N-dT were used for degrading DO. In summary, based on all the above results, it was easy to conclude that the RR of TOC during removing DO when using BZHP was higher than that when Bi_2SmSbO_7, $ZnBiYO_4$ or N-dT were used, which meant that BZHP owned the maximal mineralization percentage ratio compared with the other three photocatalysts.

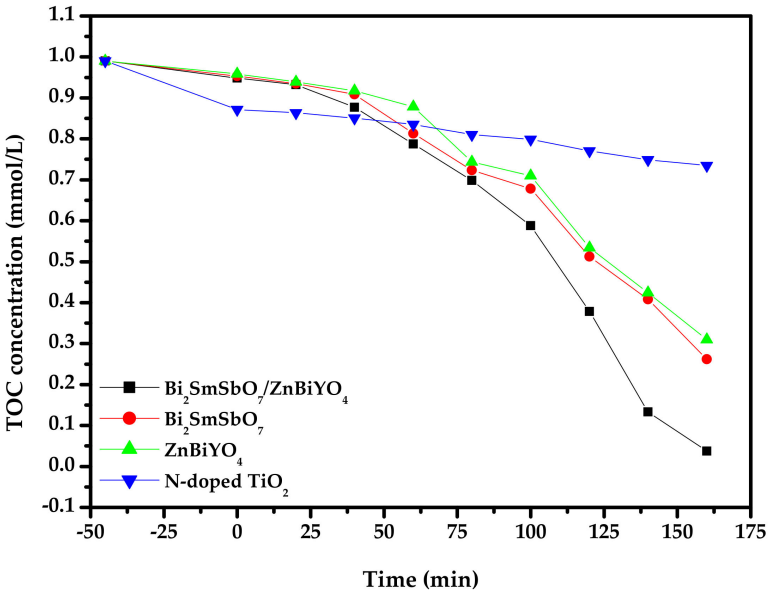

Figure 13. Concentration changing curved line of TOC during PD of DO in dye wastewater with $Bi_2SmSbO_7/ZnBiYO_4$ heterojunction or with Bi_2SmSbO_7or with $ZnBiYO_4$ or with N-doped TiO_2 as catalyst under VLI.

Figure 14 presents the concentration variation curves of DO during PD with $Bi_2SmSbO_7/ZnBiYO_4$ heterojunction as the photocatalyst under VLI for three cycle degradation (TCD) tests. Figure 14 shows that the RR of DO reached 98.03%, 96.73% or 95.43%, respectively, after VLI-160M with $Bi_2SmSbO_7/ZnBiYO_4$ heterojunction as catalyst by finishing 3 cycle experiments for removing DO. Figure 15 reveals the concentration changing curved line of TOC during PD of DO with BZH as the photocatalyst under VLI for TCD tests. We could observe from Figure 15 that the RR of TOC was 94.98%, 93.51% or 92.19%, respectively, after VLI-160M with BZH as the photocatalyst. The experimental results, which were obtained from Figures 14 and 15, showed that the BZHP had high stability.

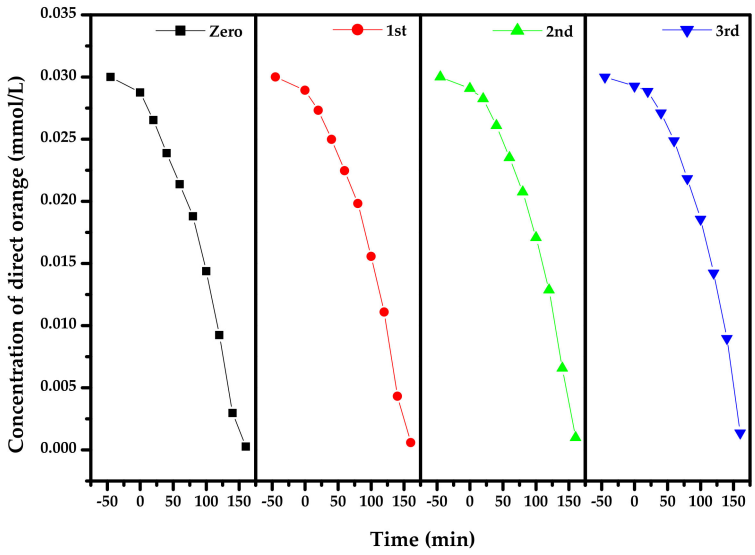

Figure 14. Concentration variation curves of DO during PD of DO in dye wastewater with $Bi_2SmSbO_7/ZnBiYO_4$ heterojunction as photocatalyst under VLI for three cycle degradation tests.

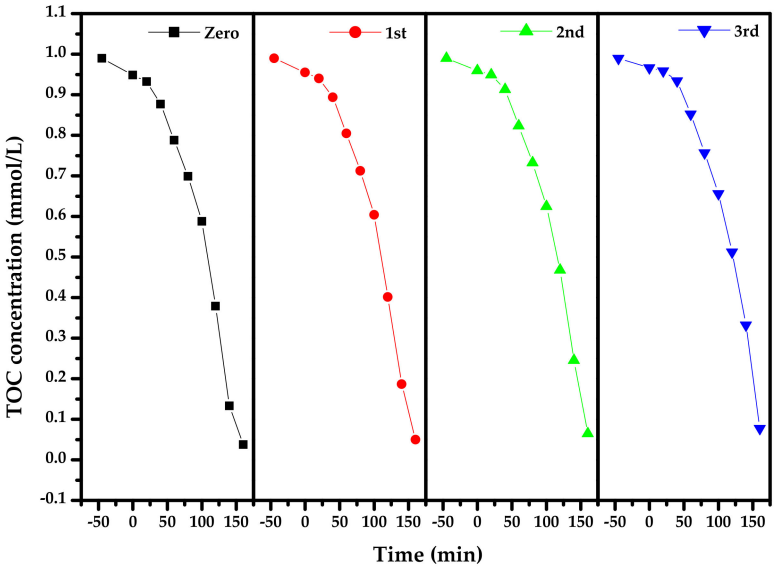

Figure 15. Concentration changing curved line of TOC during PD of DO in dye wastewater with $Bi_2SmSbO_7/ZnBiYO_4$ heterojunction as photocatalyst under VLI for 3 cyclical degradation experiments.

Figure 16 exhibits the second-order kinetic curves for the PD of DO with BZH, Bi_2SmSbO_7, $ZnBiYO_4$ or N-dT as catalysts under VLI. According to Figure 16, the dynamic constant k, which was obtained from the kinetic plot toward DO concentration and VLI time with BZH, Bi_2SmSbO_7, $ZnBiYO_4$ or N-dT as catalyst, reached 2.167 or 0.495 or 0.395 or 0.089 min^{-1}, respectively. The dynamic constant k, which derived from the kinetic plot toward TOC concentration, was 0.047 or 0.010 or 0.009 or 0.002 min^{-1} with BZH, Bi_2SmSbO_7, $ZnBiYO_4$ or N-dT as photocatalysts. The fact that the merical number of K_{TOC} for removing DO was lower than the merical number of K_C for removing DO, even though they were using the same catalyst, indicated that the photodegradation intermediate products probably appeared during the PD of DO under VLI. At the same time, the degradation of DO by BZHP showed higher mineralization efficiency compared with the other three photocatalysts.

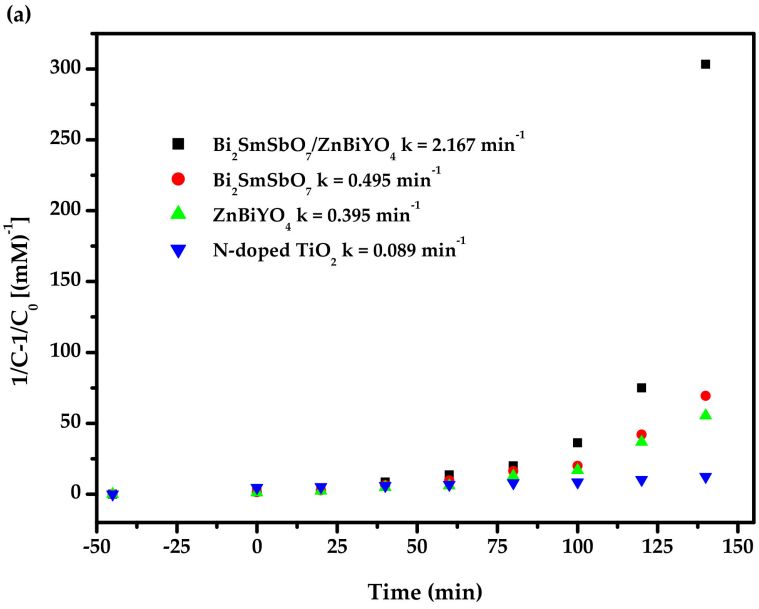

Figure 16. *Cont.*

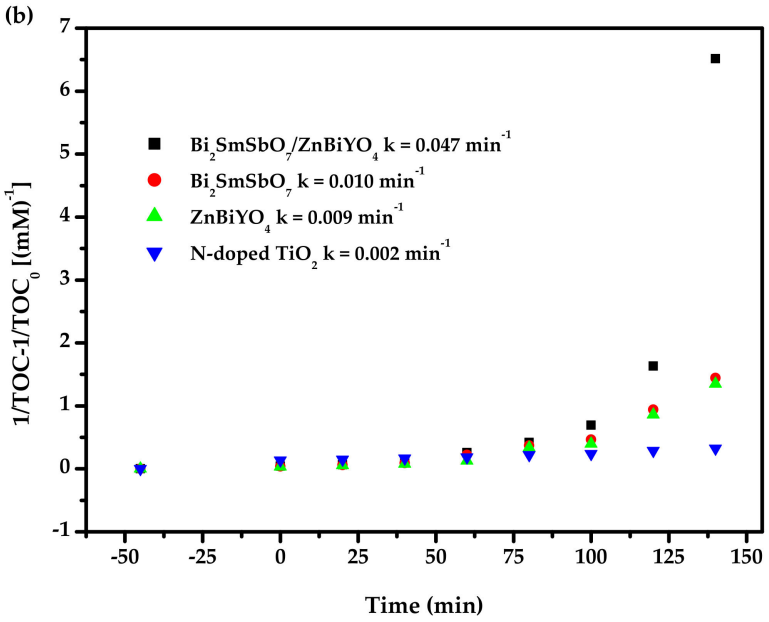

Figure 16. (**a**) Observed second-order dynamic curves for the PD of DO with $Bi_2SmSbO_7/ZnBiYO_4$ heterojunction or with Bi_2SmSbO_7 or with $ZnBiYO_4$ or with N-dT as catalyst under VLI; (**b**) Achieved second-order kinetic plots for TOC during PD of DO with BZH or with Bi_2SmSbO_7 or with $ZnBiYO_4$ or with N-dT as catalyst under VLI.

Figure 17 displays the observed second-order kinetic plots for the PD of DO with BZH as the photocatalyst under VLI for TCD tests. According to the results in Figure 17, the dynamic constant k, which was obtained from the kinetic plot towards the DO concentration and VLI time with BZH as the photocatalyst for TCD tests, was equivalent to 1.415 or 0.849 or 0.558 min^{-1}. Figure 18 shows the achieved second-order dynamic curves for TOC during the PD of DO with BZH as catalyst under VLI for TCD tests. It could be found from Figure 18 that the kinetic constant k, which came from a dynamic curve towards the TOC concentration and VLI time with BZH as the photocatalyst for TCD tests, achieved 0.031 min^{-1} or 0.022 min^{-1} or 0.014 min^{-1}. The results of Figures 16–18 exhibited that the PD of DO with BZH as the photocatalyst under VLI coincided to the second-order reaction kinetics.

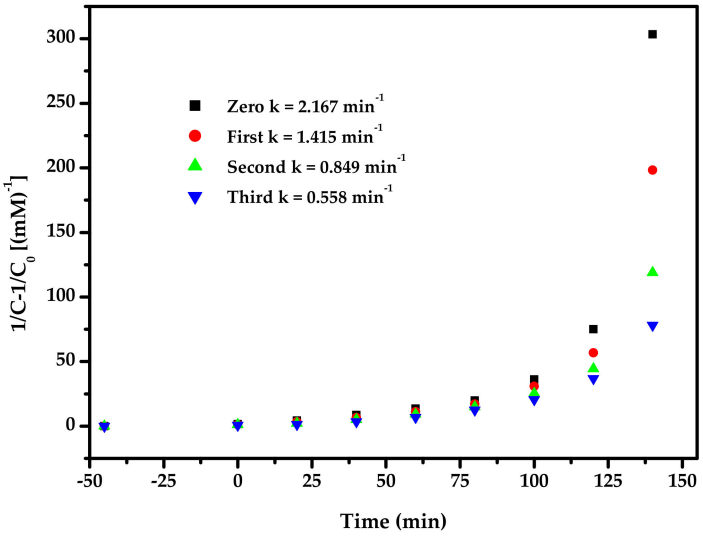

Figure 17. Achieved second-order dynamic curves for the PD of DO with $Bi_2SmSbO_7/ZnBiYO_4$ heterojunction as the photocatalyst under VLI for three cycle degradation tests.

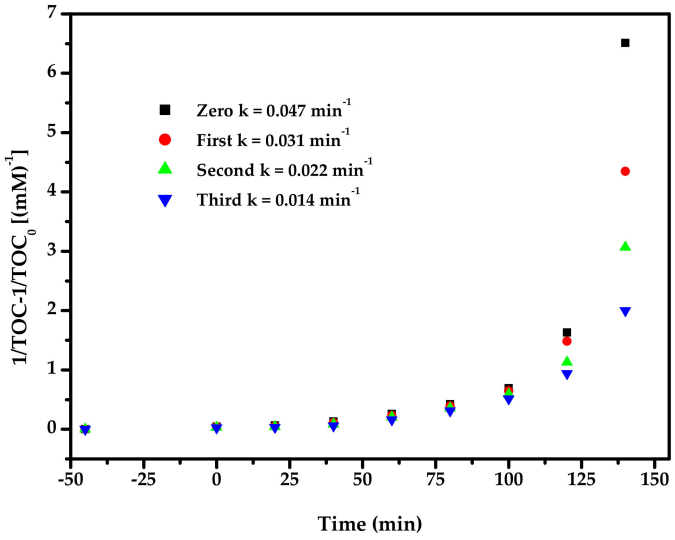

Figure 18. Observed second-order kinetic plots for TOC during the PD of DO with $Bi_2SmSbO_7/ZnBiYO_4$ heterojunction as the photocatalyst under VLI for 3 cyclical degradation experiments.

A conclusion could be summarized from Figures 17 and 18 that the RR of DO decreased by 3.67% with BZH as the photocatalyst under VLI after TCD tests and the RR of TOC decreased by 4.02%. In the above three cycle experiments, there was no significant difference in degradation efficiency, and the photocatalyst structure of BZHP was stable.

Figure 19 exhibits the relation curves among ethylenediamine tetraacetic acid (EDTA), isopropanol (IPA) or benzoquinone (BQ) and RR of DO with BZH as the catalyst under VLI. At the beginning of the photo-catalysis experiment, different free radical scavengers were added to the DO solution to capture the active species during the degradation process of DO. Isopropanol (IPA) that we used to capture hydroxyl radicals ($^{\bullet}OH$), benzoquinone (BQ) that we utilized to capture superoxide anions ($^{\bullet}O_2^-$), and ethylenediaminetetraacetic acid (EDTA) that we used to capture holes (h^+). The starting IPA concentration, BQ concentration or EDTA concentration was equivalent to 0.15 mmol L^{-1}, and the added amount of IPA or BQ or EDTA was equivalent to 1 mL. Based on Figure 19, when the IPA, BQ or EDTA was put into the DO solution, the RR of DO decreased by 67.13%, 49.87% or 27.80%, respectively, compared with the standard RR of DO. Therefore, the conclusion could be drawn that in the process of DO degradation, $^{\bullet}OH$, h^+ and $^{\bullet}O_2^-$ were all active free radicals, and $^{\bullet}OH$ played a leading role when using BZH as the photocatalyst to degrade DO under VLI. By using the experiment of adding a capture agent, it was found that the hydroxyl radical possessed the maximum oxidizing removal capability for eliminating DO in dye wastewater compared with superoxide anion or holes. The oxidizing removal capability for degradation DO was as follows: hydroxyl radical > superoxide anion > holes.

The Nyquist impedance plot measurement was an important test that was always used for characterization of the migrating course of photoinduced electrons and photoinduced holes at the solid/electrolyte separating surface of the photocatalysts. The smaller arc radius meant that the transportation efficiency of the photocatalysts was high. Figure 20 shows the corresponding Nyquist impedance plots of the prepared BZHP or Bi_2SmSbO_7 photocatalyst or $ZnBiYO_4$ photocatalyst. It was distinct, according to Figure 20, that the diameter of the arc radius was in the order $ZnBiYO_4$ > Bi_2SmSbO_7 > BZHP, as the above results indicated that BZHP exhibited a more efficient separation of photogenerated electron and photogenerated hole and faster interfacial charge migration ability.

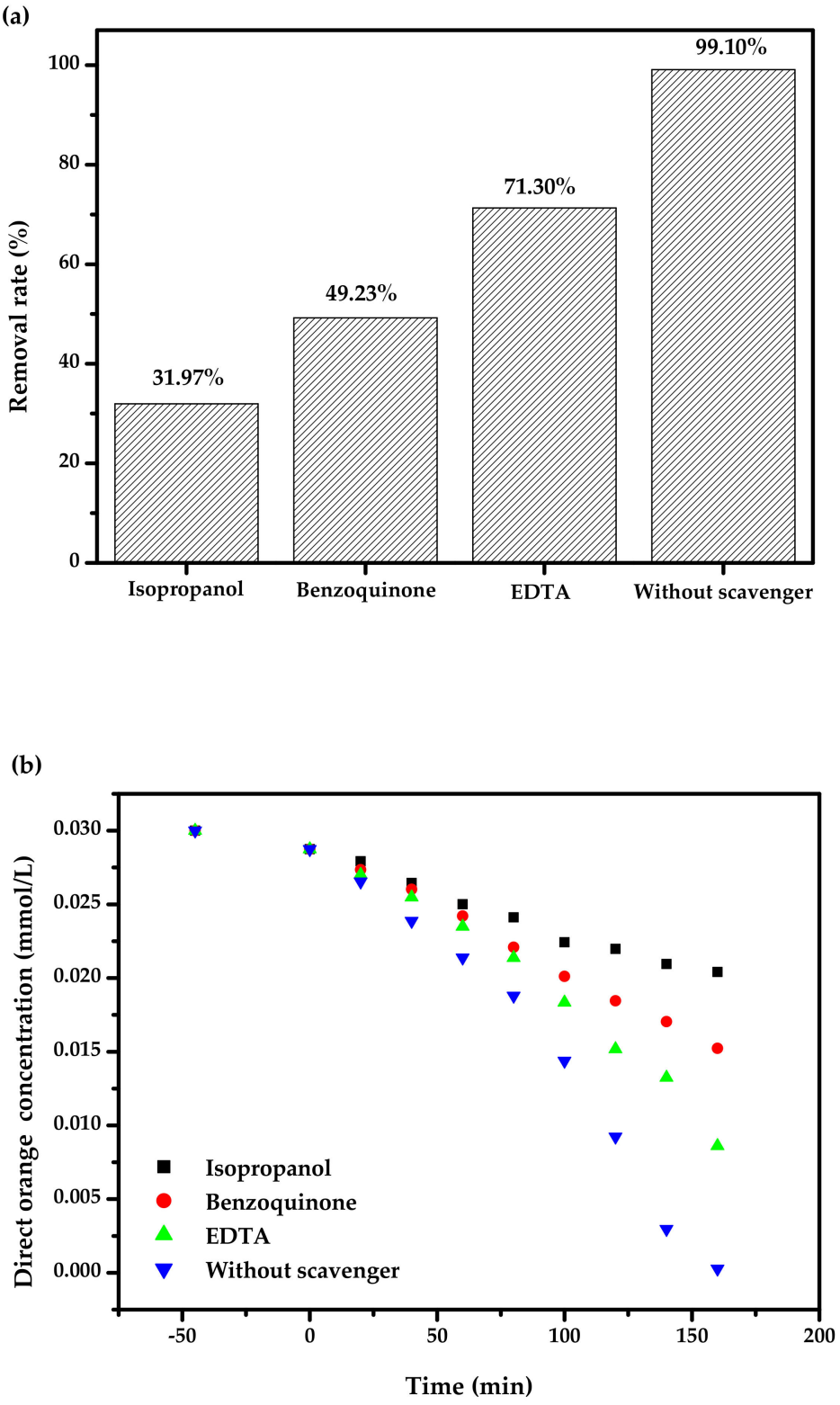

Figure 19. (**a**) RR of DO by using three trapping agents with BZH as the catalyst under VLI. (**b**) The relation curves among ethylenediamine tetraacetic acid (EDTA), isopropanol (IPA) or benzoquinone (BQ) and RR of DO with BZH as the catalyst under VLI.

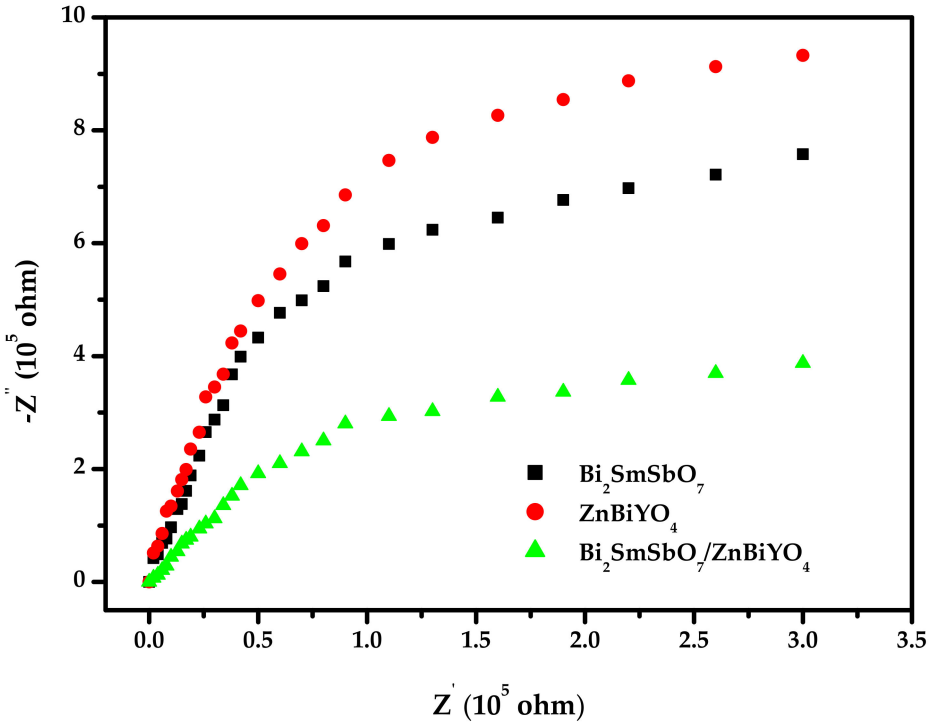

Figure 20. Nyquist impedance plots of $Bi_2SmSbO_7/ZnBiYO_4$ heterojunction photocatalyst or Bi_2SmSbO_7 photocatalyst or $ZnBiYO_4$ photocatalyst.

2.5. Probable Degradation Mechanism Analysis

The probable PD mechanism of DO with BZH as photocatalyst under VLI is exhibited in Figure 21. The potentials of the conductance band (CB) or valence bond band (VB) for quasi-conductors were estimated using the following Formulas (3) and (4) [94]:

$$E_{CB} = X - E^e - 0.5E_g \quad (3)$$

$$E_{VB} = E_{CB} + E_g \quad (4)$$

In the above two equations, E_g was the bandgap of the quasi-conductor, X was the electronegativity of the quasi-conductor and E^e was the free electronic energy on the hydrogen scale (E^e = 4.5 eV). The VB electric potential or the CB electric potential for Bi_2SmSbO_7 (determined by Formulas (3) and (4)) was equivalent to 2.539 eV or 0.123 eV, respectively. In addition, for $ZnBiYO_4$, the VB electric potential and the CB electric potential were calculated to be 1.271 eV and −0.682 eV, respectively. It could be found that both Bi_2SmSbO_7 and $ZnBiYO_4$ could assimilate seeable light and constitutionally generated electron–hole pairs when the BZHP was irradiated by VLI. Since the redox potential position of the CB of $ZnBiYO_4$ (−0.682 eV) was more negative than that of Bi_2SmSbO_7 (0.123 eV), the photoinduced electrons on the CB of $ZnBiYO_4$ could transform to the CB of Bi_2SmSbO_7. In addition, the redox potential position of the VB of Bi_2SmSbO_7 (2.539 eV) was more positive than that of $ZnBiYO_4$ (1.271 eV), the photoinduced holes on the VB of Bi_2SmSbO_7 could transfer to the VB of $ZnBiYO_4$. Hence, using BZHP, which consists of Bi_2SmSbO_7 and $ZnBiYO_4$, would obviously diminish the reunion rate of photo-induced electrons and photo-induced holes. Moreover, the inner resistance would also decrease, and the lifespan of photoinduced electrons, photo-induced holes and the interfacial charge transfer would be enhanced [95]. As a result, more $^{\bullet}OH$ or $^{\bullet}O_2^-$ (oxidative radicals) could be manufactured, helping to raise the removal efficiency of DO. In Figure 21, the CB potential of $ZnBiYO_4$ was −0.682 eV and the potential of $O_2/^{\bullet}O_2^-$ was −0.33 V, and more subtractive potential meant that the electrons within the CB of $ZnBiYO_4$ could absorb oxygen to produce $^{\bullet}O_2^-$ which could degrade DO. The value of the VB electric potential

of Bi_2SmSbO_7 was (2.539 eV) larger than that of $OH^-/{}^{\bullet}OH$ (2.38 V), revealing that the holes in the VB of Bi_2SmSbO_7 could oxidize H_2O or OH^- into $^{\bullet}OH$ for degrading DO, which was shown as path 2. Lastly, as shown in path 3, the photoinduced holes in the VB of Bi_2SmSbO_7 or $ZnBiYO_4$ could straightly oxidize and remove DO owing to its strong oxidation capability. To sum up, the high efficiency of electron–hole separation was the reason that BZHP could promote DO degradation.

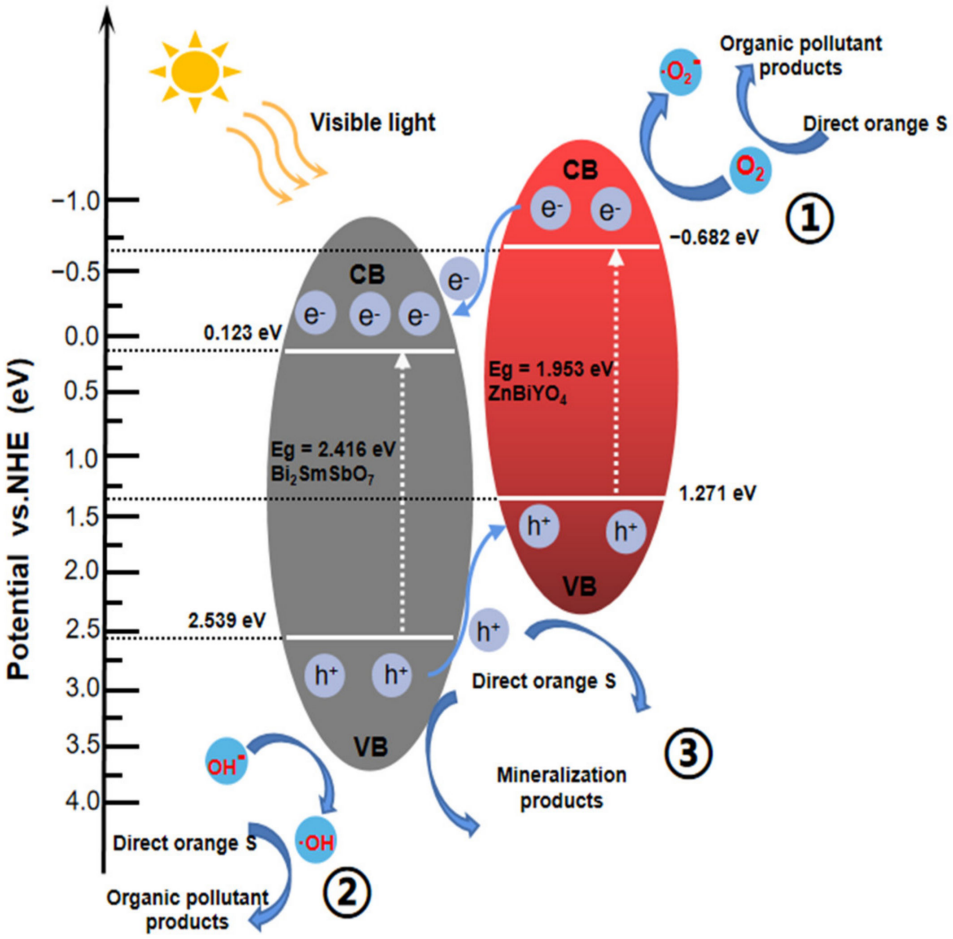

Figure 21. Possible PD mechanism of DO with $Bi_2SmSbO_7/ZnBiYO_4$ heterojunction as photocatalyst under VLI.

For the purpose of studying the degradation mechanism of DO, the intermediate products were also detected using the LC-MS method during the degradation process of DO. The intermediate products which were obtained during the PD of DO were identified as phenyldiazene (m/z = 106), naphtahlene (m/z = 127), aniline (m/z = 93), hydroquinone (m/z = 112), 1,2,6-trihydroxy-3-naphthalene sulfonate (m/z = 257), phenol (m/z = 94), oxalid acid (m/z = 90), $C_{11}H_{10}O_5N_2S$ (m/z = 282), $C_{11}H_9O_5NS$ (m/z = 266) and 8-aminonaphthol (m/z = 152). Based on the detected intermediates, we could extrapolate the degradation pathway of DO, as shown in Figure 22. It could be found from Figure 22 that oxidation reaction and hydroxylation reaction were realized during PD process of DO. Ultimately, DO was converted into small molecular organic compounds and finally united with other organic active groups to convert into carbon dioxide and water.

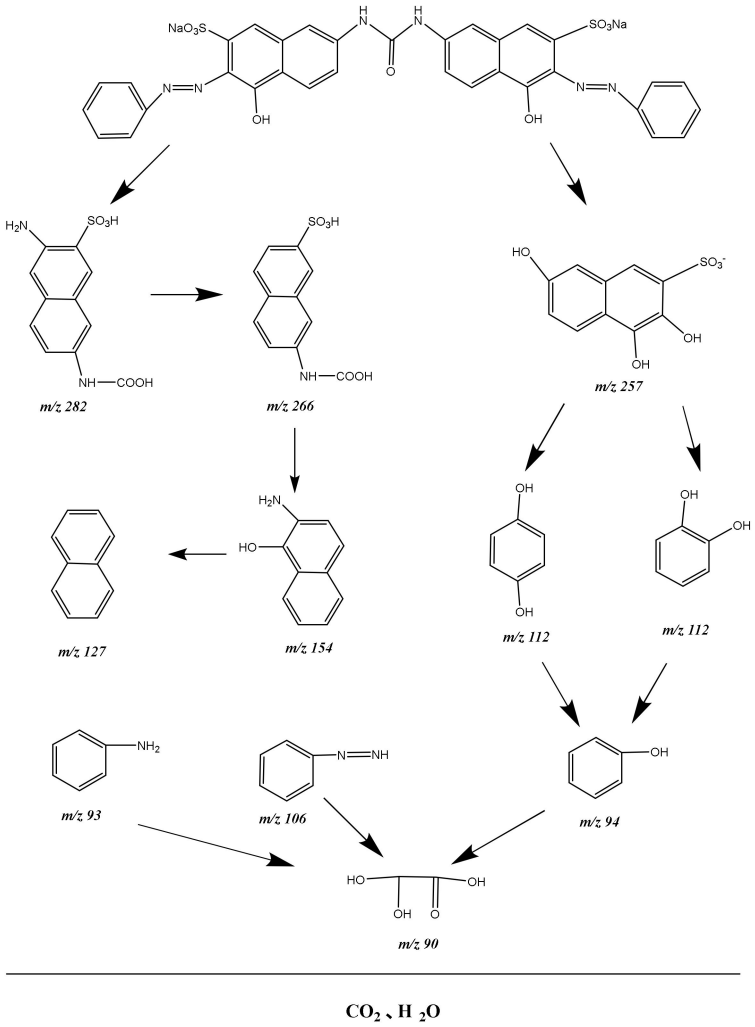

Figure 22. Suggested PD pathway scheme for DO under VLI with $Bi_2SmSbO_7/ZnBiYO_4$ heterojunction as catalyst.

3. Experimental Section

3.1. Materials and Reagents

The analytical grades were ethylenediaminetetraacetic acid (EDTA, 99.5%), isopropyl alcohol (IPA, purity ≧ 99.7%) and *P*-benzoquinone (BQ, purity ≧ 98.0%). The purchased anhydrous ethanol (purity ≧ 99.5%) conformed to the specifications of the American Chemical Society. The gas chromatography grade was DO (chemical formula: $C_{33}H_{22}N_6Na_2O_9S_2$, purity ≧ 98%). In this work, ultra-pure water (18.25 MU cm) was utilized.

3.2. Preparation Method of Bi_2SmSbO_7

The new photocatalyst Bi_2SmSbO_7 was synthesized via a high-temperature solid-phase sintering method at a temperature of 1090 °C. High purity Bi_2O_3 (99.99%), Sm_2O_3 (99.99%) and Sb_2O_5 (99.99%) were used for raw materials. Because all the raw materials were of high purity, it was unnecessary to do the further purification test. Due to the high volatility of Bi_2O_3 at high temperatures, we finally decided to increase the amount of Bi_2O_3 to 120% after 5 experiments. Before the experiment, all the above powders ($n(Bi_2O_3)$:$n(Sm_2O_3)$:$n(Sb_2O_5)$ = 2.4:1:1) were dried for 4 h at 200 °C. The Bi_2SmSbO_7 was prepared by mixing the precursors stoichiometrically, then pressing them into small columns and putting them in an alumina crucible. After calcination in an electric furnace for 2 h at 400 °C, the raw materials and small columns were taken out. We ground the

mixture and then put them in the electric stove. Finally, it was calcined separately in an electric furnace at 1090 °C for 35 h.

The 0.30 mol/L Bi $(NO_3)_3 \cdot 5H_2O$, 0.15 mol/L $Sm(NO_3)_3 \cdot 6H_2O$ and 0.15 mol/L $SbCl_5$ were blended and kept stirring for 20 h. The above solution was transferred to an autoclave lined with polytetrafluoroethylene and heated at 200 °C for 15 h. Afterwards, the achieved powder was calcined in a tubular stove at 8 °C/min under N_2 for 10 h at 800 °C. Finally, Bi_2SmSbO_7 powder was also obtained by the hydrothermal synthesis method.

3.3. Preparation Method of $ZnBiYO_4$

Preparation of the $ZnBiYO_4$ catalyst was realized by high-temperature solid-phase sintering method. ZnO, Bi_2O_3 and Y_2O_3 were all raw materials with a purity as high as 99.99%. Due to the high volatility of Bi_2O_3 at high temperatures, we finally decided to increase the amount of Bi_2O_3 to 120% after 5 experiments. In order to decrease the particle size of the fully-mixed materials (n(ZnO): $n(Bi_2O_3)$: $n(Y_2O_3)$ = 2.4:1:1), a ball mill method was used for making the final particle size to 1–2 μm. Before the synthesis of the target products, all the powder compounds were dried at 200 °C for 4 h. These powders were pressed into discs and put into an alumina crucible in an electric stove (KSL1700X, Hefei Kejing Materials Technology Co., Ltd., Hefei, China) and heated at 750 °C for 6 h. The powder was heated again in the same electric furnace at 1000 °C for 35 h after the pressing and crushing procedures. Lastly, after complete grinding, pure $ZnBiYO_4$ catalyst was obtained.

The 0.15 mol/L $Zn(NO_3)_2 \cdot 6H_2O$, 0.15 mol/L Bi $(NO_3)_3 \cdot 5H_2O$ and 0.15 mol/L $Y(NO_3)_3 \cdot 6H_2O$ were mixed and kept stirring for 20 h. The above solution was transferred to an autoclave lined with polytetrafluoroethylene and heated for 15 h at 200 °C. Then, the resultant powder was calcined in a tubular stove at a rate of 8 °C per min under N_2 protection at 780 °C for 10 h. Finally, $ZnBiYO_4$ powder was also obtained by hydrothermal synthesis method.

3.4. Synthesis of N-Doped TiO_2

The nitrogen-doped titanium dioxide (NT) catalyst used tetrabutyl titanate as the precursor, ethanol as the solvent, and was prepared by the sol-gel method. The operation steps were as follows: the first step was to mix 17 mL of tetrabutyl titanate with 40 mL of absolute ethanol to form solution A; 40 mL of absolute ethanol, 10 mL of glacial acetic acid and 5 mL of double distilled water were mixed to make solution B. Under stirring conditions, solution A was mixed dropwise into the solution to form a transparent colloidal suspension (TCS). In the second step, under magnetic stirring conditions, ammonia water with an N/Ti ratio of 8 mol% was mixed with the obtained TCS for 1 h. In the third step, a xerogel was formed after aging for two days. The dry gel was ground into powder and calcined for 2 h at 500 °C. In the final step, we ground the powder in the agate mortar and sieved it through a vibrating screen to acquire NT powder.

3.5. Synthesis of $Bi_2SmSbO_7/ZnBiYO_4$ Heterojunction Photocatalyst

The maximum calcination temperature of $ZnBiYO_4$ which was prepared by the solid-state sintering method was 1000 °C and the heat retaining time was 35 h. The maximum calcination temperature of Bi_2SmSbO_7, which was prepared by the solid-state sintering method was 1090 °C and the heat retaining time, was 35 h. The highest calcination temperature of $ZnBiYO_4$ which was prepared by the hydrothermal synthesis method was 780 °C, and the heat retaining time was 10 h. The maximum calcination temperature of Bi_2SmSbO_7, which was prepared by hydrothermal synthesis method, was 800 °C and the heat retaining time was 10 h. On the one hand, the higher the maximum calcination temperature was, the greater the power energy consumption was, which would reduce and consume the service life of the furnace instrument. On the other hand, the longer heat retaining time and the higher maximum sintering temperature would cause the larger particle size of $ZnBiYO_4$ or Bi_2SmSbO_7. As a result, the specific surface area of $ZnBiYO_4$ or

Bi_2SmSbO_7 would be reduced and the photocatalytic activity of $ZnBiYO_4$ or Bi_2SmSbO_7 would be correspondingly decreased. In order to improve the photocatalytic activity, reduce energy consumption and improve the instrument life of high-temperature calciner, we used the hydrothermal synthesis method to prepare $ZnBiYO_4$ and Bi_2SmSbO_7 in the process of preparing heterojunction.

First, solution Bi $(NO_3)_3 \cdot 5H_2O$ (0.30 mol/L), solution $Sm(NO_3)_3 \cdot 6H_2O$ (0.15 mol/L) and solution $SbCl_5$ (0.15 mol/L) were mixed and kept stirring for 20 h. The above solution was transferred to an autoclave lined with polytetrafluoroethylene and heated at 200 °C for 15 h. Afterwards, the achieved powder was calcined at 800°C for 10 h in a tubular stove at a rate of 8 °C per minute under N_2 protecting. Bi_2SmSbO_7 powder was obtained by hydrothermal synthesis method. Secondly, solution $Zn(NO_3)_2 \cdot 6H_2O$ (0.15 mol/L), solution Bi $(NO_3)_3 \cdot 5H_2O$ (0.15 mol/L) and solution $Y(NO_3)_3 \cdot 6H_2O$ (0.15 mol/L) were mixed and kept stirring for 20 h. The above solution was transferred into an autoclave lined with polytetrafluoroethylene and heated at 200 °C for 15 h. Then, the achieved powder was calcined at 780 °C for 10 h in a tubular stove at a rate of 8 °C per minute under N_2 protecting. $ZnBiYO_4$ powder was obtained by hydrothermal synthesis method. The individual photocatalysts, such as $ZnBiYO_4$ or Bi_2SmSbO_7, were prepared by hydrothermal synthesis method.

In this text, a new catalyst BZHP was synthesized by solvothermal method. BZHP was prepared by mixing 890 mg Bi_2SmSbO_7 and 30 wt.% (610 mg) $ZnBiYO_4$ in 300 mL of octanol ($C_8H_{18}O$) and the above mixture was dispersed in an ultrasonic bath for 1 h. Then, under vigorous stirring conditions, the mixture was heated to reflux at 140 °C for 2 h to improve the adhesion of $ZnBiYO_4$ on the surface of Bi_2SmSbO_7 nanoparticles and BZHP was formed. First, the catalyst was naturally cooled to room temperature, then the products were collected by centrifugation method and washed with a hexane / ethanol mixture. After the powder was purified, the powder was dried in a 60 °C vacuum oven for 6 h and laid in a desiccator for later use. Finally, BZHP was prepared successfully.

3.6. Characterizations

The structure of the samples was analyzed using a powder XRD test (Cu Kαradiation, λ = 1.54184 Å, preset time of 0.3 s $step^{-1}$, step length of 0.02°). A scanning electron microscope (SEM) was used to characterize the morphology and microstructure of the prepared samples and the elementary composition, which was derived from above prepared samples, was obtained by energy dispersive spectroscopy (EDS). The diffuse reflectance spectra of the above prepared samples were obtained by UV-Vis spectrophotometer (UV-Vis DRS, UV-3600). Valence analysis and chemical composition of surface for the catalysts were realized by X-ray photoelectron spectrograph (XPS) with an Al-kα X-ray source.

3.7. Photoelectrochemical Experiments

The electrochemical impedance spectroscopy experiment was performed by the CHI660D electrochemical station with standard 3 electrodes. In this system, the working electrode, counter electrode and reference electrode are prepared catalyst, platinum plate and commercial Ag/AgCl electrode, respectively. An aqueous solution of Na_2SO_4 (0.5 mol/L) was used as the electrolyte, and a 500 W xenon lamp with an ultraviolet cut-off filter was used as the visible light lamp for photochemical measurement. The working electrode was prepared by the following method: Dissolved 0.03 g of the sample and 0.01 g of chitosan in 0.45 mL of dimethylformamide, and to form a uniform suspension after ultrasonic treatment for 1 h. Subsequently, they were dropped on indium tin oxide (ITO) conductive glass with a size of 1 cm × 2 cm. Finally, we dried the working electrode at 80 °C, which lasted for 10 min.

3.8. Experimental Setup and Procedure

The temperature of the experimental reaction system was 20 °C (reactive vessel, XPA-7, Xujiang Electromechanical Plant, Nanjing, China), which was regulated by circulating

cooling water. The simulated daylight illumination consists of a 500 W xenon lamp and a 420 nm cut-off filter. There were 12 same quartz tubes (40 mL). The dosage of Bi_2SmSbO_7 or $ZnBiYO_4$ or BZHP was equivalent to 0.75 g/L. Moreover, the concentration of DO was equivalent to 0.03 mmol/L. The DO concentration was the residuary concentration of actual dye wastewater after biodegradation, and the content of DO was equivalent to 1.2 mmol/L. During the reaction, 3 mL of suspension was withdrawn termly. Subsequently, the filtration was realized for removing the catalyst. Ultimately, the residuary concentration of DO in solution was defined by the UV-Vis spectrophotometer (Shimadzu, UV-2450, Shimadzu Corporation Co., Ltd., Chengdu, China). The absorption wavelength (detecting wavelength) of DO was 665 nm. The absorbance standard curve of DO at different concentrations was accomplished under ultraviolet light irradiation in the range of 220 nm–320 nm with an ultraviolet-visible spectrophotometer. The relationship between the concentration of DO and the absorbance value at 665 nm should be calculated. The absorbance of DO in the solution was measured at the absorption wavelength of 665 nm, the calibration curve of DO was drawn and a linear regression method was used for the quantification of DO. Before VLI, the suspension containing photocatalyst and DO was magnetically stirred in the dark for 45 min to establish adsorption/desorption equilibrium among photocatalyst, DO and O_2. During the VLI, the suspension was agitated at 500 rpm.

Experimental data of mineralization of DO in reaction solution were meteraged. In order to examine the TOC concentration during the process of PD of DO, potassium phthalate ($KHC_8H_4O_4$) or anhydrous sodium carbonate was used as a standardized agent. Potassium phthalate standard solutions with carbon concentration (0–100 mg/L) were prepared for calibration purpose. Each time, we used 6 samples (45 mL) to measure TOC concentration.

Liquid chromatography-mass spectrometry was used to identify and measure DO, and its intermediate degradation products. Then, the 20 μL solution which was acquired after the photocatalytic reactivity was automatically injected. The flow rate was 0.2 mL/min, which was a mobile phase containing 60% methanol and 40% ultrapure water. Electrospray ionization interface (27 °C, 19.00 V), spray voltage of 5000 V, and constant sheath gas flow rate were MS conditions. Spectra were acquired in the m/z range from 50 to 600 in negative ion scan mode.

In order to measure the photon intensity of incident light, the filter, which was 7 centimeters in length and 5 cm in width, was chosen to be irradiated by incident single-wavelength visible light of 420 nm. According to the formula of $\upsilon = c/\lambda$ and $h\upsilon$, which represented the energy of a photon, Avogadro constant N_A, Planck constant h, photonic frequency υ, incident light wavelength λ and light velocity c were used to obtain the mole number of the total photons or the reactive photons which passed through the total area of above filter per unit time. The length between the xenon lamp and the light reactor was adjusted. As a result, the incident photon flux on the photoreactor was changed.

We estimated the photon efficiency according to the following Formula (5):

$$\varphi = \frac{R}{I_0} \tag{5}$$

In this formula, ϕ presented the photonic efficiency (%), R presented the degradation rate of DO (mol L^{-1} s^{-1}), and I_o presented the incident photon flux (Einstein L^{-1} s^{-1}). The incident photon flux I_o was measured by a radiometer under VLI. ($I_o = 4.76 \times 10^{-6}$ Einstein L^{-1} s^{-1}.)

4. Conclusions

For the first time, the Bi_2SmSbO_7 compound was successfully synthesized by two methods: the hydrothermal synthesis method and solid state method with high temperature. BZHP was proposed and synthesized with the solvothermal method for degrading DO in dye wastewater. The photophysical properties of the single phase Bi_2SmSbO_7 and BZH were investigated. In interpreting the results, the following conclusions could be easily obtained. Bi_2SmSbO_7 compound was a pure phase which crystallized in a pyrochlore

structure that belonged to a cubic crystal system with the space group *Fd3m*. The lattice parameter a = 10.835(1) Å, and the BGE of Bi_2SmSbO_7 was 2.42 eV. BZHP was certified to be an efficient photocatalyst for remedying DO in the dye wastewater, after VLI-160M, the RR of DO was as high as 99.10%, and the RR of TOC was 96.21%. BZH showed the best performance in removing DO, the RR with BZH as the catalyst was equivalent to 1.200 or 1.268 or 3.019 times higher than the RR with Bi_2SmSbO_7 as the catalyst, $ZnBiYO_4$ as the catalyst or with N-dT as the catalyst. Therefore, the study with BZH as the catalyst provided a new idea for the treatment of dye wastewater that contained DO and it could also promote the property improvement of the photocatalyst in the future.

Author Contributions: Conceptualization, J.L.; data curation, J.L., B.M., Z.W. and B.N.; formal analysis, J.L., B.M., Y.Y. and B.N.; investigation, J.L., B.M. and B.N.; methodology, J.L., B.M., W.L. and B.N.; resources, J.L.; software, J.L., G.Y. and W.L.; visualization, J.L., Y.Y. and G.Y.; writing—original draft preparation, J.L., B.M., Z.W., Y.Y. and B.N.; writing—review and editing, J.L.; validation, J.L., B.M., Z.W., W.L. and G.Y. All authors have read and agreed to the published version of the manuscript.

Funding: This study was supported by the Project Funded by the Scientific and Technical Innovation Leading Personnel and Team Foundation for Middle-aged and Young Scientist of Science and Technology Bureau of Jilin Province of China (Grant No. 20200301033RQ), by the Free Exploring Key Item of Natural Science Foundation of Science and Technology Bureau of Jilin Province of China (Grant No. YDZJ202101ZYTS161), by the Industrial Technology Research and Development Fund of Jilin Province Capital Development Fund on Budget in 2021 of Jilin Province Development and Reform Commission of China (Grant No. 2021C037-1), by the Innovational and Enterprising Talents of Department of Human Resource and Social Security of Jilin Province of China (Grant No. 2020033), by Natural Science Foundation of Changchun Normal University (Grant No. [2019]13), by the Scientific Research Initiating Foundation for Advanced Doctor of Changchun Normal University.

Acknowledgments: This study was supported by the Scientific and Technical Innovation Leading Personnel and Team Foundation for Middle-aged and Young Scientist of Science and Technology Bureau of Jilin Province of China (Grant No. 20200301033RQ), by the Free Exploring Key Item of Natural Science Foundation of Science and Technology Bureau of Jilin Province of China (Grant No. YDZJ202101ZYTS161), by the Industrial Technology Research and Development Fund of Jilin Province Capital Development Fund on Budget in 2021 of Jilin Province Development and Reform Commission of China (Grant No. 2021C037-1), by the Innovational and Enterprising Talents of Department of Human Resource and Social Security of Jilin Province of China (Grant No. 2020033), by Natural Science Foundation of Changchun Normal University (Grant No. [2019]13), by the Scientific Research Initiating Foundation for Advanced Doctor of Changchun Normal University.

Conflicts of Interest: The authors declare no conflict of interest.

References

1. Meng, Z.L.; Zhang, Y.H.; Zhang, Z.L.; Zhang, Q.; Chu, P.K.; Komarneni, S.; Lv, F.Z. Anomalous but massive removal of two organic dye pollutants simultaneously. *J. Hazard. Mater.* **2016**, *318*, 54–60. [CrossRef] [PubMed]
2. Rathi, B.S.; Kumar, P.S.; Vo, D.V.N. Critical review on hazardous pollutants in water environment: Occurrence, monitoring, fate, removal technologies and risk assessment. *Sci. Total Environ.* **2021**, *797*, 149134. [CrossRef] [PubMed]
3. Shen, Z.Z.; Shen, H.Z. Ultrasound enhancement of the reduction of the Basic Green dye in wastewater by cast iron. *J. Environ. Sci.* **2006**, *18*, 1–3.
4. Qamar, M.; Saquib, M.; Muneer, M. Photocatalytic degradation of two selected dye derivatives, chromotrope 2B and amido black 10B, in aqueous suspensions of titanium dioxide. *Dye. Pigment.* **2005**, *65*, 1–9. [CrossRef]
5. Jeevanantham, S.; Saravanan, A.; Hemavathy, R.V.; Kumar, P.S.; Yaashikaa, P.R.; Yuvaraj, D. Removal of toxic pollutants from water environment by phytoremediation: A survey on application and future prospects. *Environ. Technol. Inno.* **2019**, *13*, 264–276. [CrossRef]
6. Parvathi, V.P.; Parimaladevi, R.; Sathe, V.; Mahalingam, U. Graphene boosted silver nanoparticles as surface enhanced Raman spectroscopic sensors and photocatalysts for removal of standard and industrial dye contaminants. *Sensor. Actuat. B-Chem.* **2019**, *281*, 679–688.
7. Kasten, F.H. Cytochemical studies with acridine orange and the influence of dye contaminants in the staining of nucleic acids. *Int. Rev. Cytol.* **1967**, *21*, 141–202.
8. Zhao, S.G.; Yang, F.; Kong, F.; Li, B.F.; Xue, Z.L.; Wang, T. Decolorization of azo-type dye Direct Orange S catalyzed by laccase /mediator system. *Chin. J. Environ. Eng.* **2016**, *10*, 3912–3918.

9. He, G.L.; Zhang, Y.T. BPNN simulating photocatalytic degradation of direct orange S. *Comput. Appl. Chem.* **2008**, *25*, 1359–1364.
10. Zhong, J.B.; Li, J.Z.; Zeng, F.C. Photocatalytic Decolorization of Direct Orange S Solution by Phospho-tungstic Acid. *J. Sichuan Nor. Univ.* **2013**, *36*, 618–621.
11. Yao, P.; Xing, T.L.; Chen, G.Q. Biosynthesis of Eucommia ulmoides silver nanoparticles and application thereof in reductive catalytic degradation of Direct Orange 26. *J. Text. Res.* **2018**, *39*, 104–110.
12. Safa, Y.; Bhatti, H.N.; Bhatti, I.A.; Asgher, M. Removal of direct red-31 and direct orange-26 by low cost rice husk: Influence of immobilisation and pretreatments. *Can. J. Chem. Eng.* **2011**, *89*, 1554–1565. [CrossRef]
13. Karthikeyeni, S.; Vijayakumar, T.S.; Vasanth, S.; Ganesh, A.; Vignesh, V.; Akalya, J.; Thirumurugan, R.; Subramanian, P. Decolourisation of Direct Orange S dye by ultra sonication using iron oxide nanoparticles. *J. Exp. Nanosci.* **2015**, *10*, 199–208. [CrossRef]
14. Jadhav, J.P.; Phugare, S.S.; Dhanve, R.S.; Jadhav, S.B. Rapid biodegradation and decolorization of Direct Orange 39 (Orange TGLL) by an isolated bacterium Pseudomonas aeruginosa strain BCH. *Biodegradation* **2010**, *21*, 453–463. [CrossRef]
15. Wolf, J.H.; Korf, J. 4-bromomethyl-7-methoxycoumarin and analogs as derivatization agents for high-performance liquid-chromatography determinations—A Review. *J. Pharmaceut. Biomed.* **1992**, *10*, 99–107. [CrossRef]
16. Rasheed, T.; Nabeel, F.; Bilal, M.; Iqbal, H.M.N. Biogenic synthesis and characterization of cobalt oxide nanoparticles for catalytic reduction of direct yellow-142 and methyl orange dyes. *Biocaral. Agr. Biotechnol.* **2019**, *19*, 101154. [CrossRef]
17. Vasudevan, S.; Oturan, M.A. Electrochemistry: As cause and cure in water pollution-an overview. *Environ. Chem. Lett.* **2014**, *12*, 97–108. [CrossRef]
18. Vecitis, C.D.; Gao, G.D.; Liu, H. Electrochemical Carbon Nanotube Filter for Adsorption, Desorption, and Oxidation of Aqueous Dyes and Anions. *J. Phys. Chem.* **2011**, *115*, 3621–3629. [CrossRef]
19. Bao, N.; Li, Y.; Yu, X.H.; Niu, J.J.; Wu, G.L.; Xu, X.H. Removal of anionic azo dye from aqueous solution via an adsorption-photosensitized regeneration process on a TiO_2 surface. *Environ. Sci. Pollut. Res.* **2013**, *20*, 897–906. [CrossRef]
20. Srivastava, R.K.; Huang, S.S.; Dong, M.Z. Asphaltene deposition during CO_2 flooding. *Spe Prod. Facil.* **1999**, *14*, 235–245. [CrossRef]
21. Abejon, A.; Garea, A.; Irabien, A. Arsenic removal from drinking water by reverse osmosis: Minimization of costs and energy consumption. *Sep. Purif. Technol.* **2015**, *144*, 46–53. [CrossRef]
22. Bofill-Mas, S.; Rusinol, M. Recent trends on methods for the concentration of viruses from water samples. *Curr. Opin. Environ. Sci. Health* **2020**, *16*, 7–13. [CrossRef]
23. Luan, J.F.; Shen, Y.; Li, Y.Y.; Paz, Y. The Structural, Photocatalytic Property Characterization and Enhanced Photocatalytic Activities of Novel Photocatalysts Bi_2GaSbO_7 and Bi_2InSbO_7 during Visible Light Irradiation. *Materials* **2016**, *9*, 801. [CrossRef]
24. Fujishima, A.; Honda, K. Electrochemical photolysis of water at a semiconductor electrode. *Nature* **1972**, *238*, 37–38. [CrossRef]
25. He, J.Y.; Jia, Q.M.; Wu, S.S.; Lv, H.T.; Shan, S.Y. Application of photocatalysis in wastewater treatment. *New Chem. Mater.* **2014**, *42*, 230–232.
26. Ren, G.M.; Han, H.T.; Wang, Y.X.; Liu, S.T.; Zhao, J.Y.; Meng, X.C.; Li, Z.Z. Recent Advances of Photocatalytic Application in Water Treatment: A Review. *Nanomaterials* **2021**, *11*, 1804. [CrossRef]
27. Bora, T.; Dutta, J. Applications of Nanotechnology in Wastewater Treatment-A Review. *J. Nanosci. Nanotechno.* **2014**, *14*, 613–626. [CrossRef]
28. Xu, B.T.; Ahmed, M.B.; Zhou, J.L.; Altaee, A.; Wu, M.H.; Xu, G. Photocatalytic removal of perfluoroalkyl substances from water and wastewater: Mechanism, kinetics and controlling factors. *Chemosphere* **2017**, *189*, 717–729. [CrossRef]
29. Akpotu, S.O.; Oseghe, E.O.; Ayanda, O.S.; Skelton, A.A.; Msagati, T.A.M.; Ofomaja, A.E. Photocatalysis and biodegradation of pharmaceuticals in wastewater: Effect of abiotic and biotic factors. *Clean Technol. Environ.* **2019**, *21*, 1701–1721. [CrossRef]
30. Xu, J.; Wan, Y.P.; Huang, Y.L.; Wang, Y.R.; Qin, L.; Seo, H.J. Layered oxide semiconductor $In_2Fe_2CuO_7$: Optical properties and visible-light responsive photocatalytic abilities. *Mater. Lett.* **2016**, *179*, 175–178. [CrossRef]
31. Bu, Y.Y.; Chen, Z.Y.; Sun, C.J. Highly effificient Z-Scheme $Ag_3PO_4/Ag/WO_3$ -x photocatalyst for its enhanced photocatalytic performance. *Appl. Catal. B* **2015**, *179*, 363–371. [CrossRef]
32. Zhao, B.; Wang, M.; Lin, L.; Zeng, Q.Q.; He, D.N. Synthesis of parallel squared nanosheet-assembled Bi_2WO_6 microstructures under alkalescent hydrothermal treatment. *Ceram. Int.* **2014**, *40*, 5831–5835. [CrossRef]
33. Alemi, A.A.; Kashfifi, R.; Shabani, B. Preparation and characterization of novel Ln (Gd^{3+}, Ho^{3+} and Yb^{3+})-doped Bi_2MoO_6 with Aurivillius layered structures and photocatalytic activities under visible light irradiation. *J. Mol. Catal. A Chem.* **2014**, *392*, 290–298. [CrossRef]
34. Nazim, S.; Kousar, T.; Shahid, M.; Khan, M.A.; Nasar, G.; Sher, M.; Warsi, M.F. New graphene-CoxZn1 -xFe_2O_4 nano-heterostructures: Magnetically separable visible lightphotocatalytic materials. *Ceram. Int.* **2016**, *42*, 7647–7654. [CrossRef]
35. Ghaffar, I.; Warsi, M.F.; Shahid, M.; Shakir, I. Unprecedented photocatalytic activity of carbon coated/MoO_3 core-shell nanoheterostructurs under visible light irradiation. *Phys. E Low-Dimens. Syst. Nanostruct.* **2016**, *79*, 1–7. [CrossRef]
36. Kiransan, M.; Khataee, A.; Karaca, S.; Sheydaei, M. Artifificial neural network modeling of photocatalytic removal of a disperse dye using synthesized of ZnO nanoparticles on montmorillonite. *Spectrochim. Acta A* **2015**, *140*, 465–473. [CrossRef]
37. Khataee, A.; Karimi, A.; Arefifi-Oskoui, S.; Soltani, R.D.C.; Hanifehpour, Y.; Soltani, B.; Joo, S.W. Sonochemical synthesis of Pr-doped ZnO nanoparticles for sonocatalytic degradation of Acid Red 17. *Ultrason. Sonochem.* **2015**, *22*, 371–381. [CrossRef]
38. Yi, X.; Li, J.L. Synthesis and optical property of $NaTaO_3$ nanofifibers prepared by electrospinning. *J. Sol-Gel Sci. Technol.* **2010**, *53*, 480–484. [CrossRef]

39. Yang, J.X.; Akbarzadeh, J.; Maurer, C.; Peterlik, H.; Schubert, U. Sol-gel synthesis of $ZnTiO_3$ using a single-source precursor based on p-carboxybenzaldehyde oxime as a linker. *J. Mater. Chem.* **2012**, *22*, 24034–24041. [CrossRef]
40. Suresh, R.; Giribabu, K.; Manigandan, R.; Munusamy, S.; Kumar, S.P.; Muthamizh, S.; Stephen, A.; Narayanan, V. Doping of Co into V_2O_5 nanoparticles enhances of methylene blue. *J. Alloy. Compd.* **2014**, *598*, 151–160. [CrossRef]
41. Ge, L.; Zhang, X.H. Synthesis of novel visible light driven BiVO4 photocatalysts via microemulsion process and its photocatalytic performance. *J. Inorg. Mater.* **2009**, *24*, 453–456. [CrossRef]
42. Han, Q.F.; Chen, L.; Wang, M.J.; Yang, X.J.; Lu, L.D.; Wang, X. Low-temperature synthesis of uniform Sb_2S_3 nanorods and its visible-light-driven photocatalytic activities. *Mater. Sci. Eng. B* **2010**, *166*, 118–121. [CrossRef]
43. Yi, X.F.; Zheng, J.S.; Zhao, Y.B. Hydrothermal synthesis of CdS nanorods in NaOH solution. Chem. *J. Chin. Univ.* **2012**, *33*, 2597–2603.
44. Yang, S.X.; Yue, Q.; Wu, F.M.; Huo, N.J.; Chen, Z.H.; Yang, J.H.; Li, J.B. Synthesis of the nanostructured Cd_4GeS_6 photocatalysts and their visible-light-driven photocatalytic degradation property. *J. Alloy. Compd.* **2014**, *597*, 91–94. [CrossRef]
45. Wu, W.M.; Lin, R.; Shen, L.J.; Liang, R.W.; Yuan, R.S.; Wu, L. Visible-light-induced photocatalytic hydrogenation of 4-nitroaniline over In_2S_3 photocatalyst in water. *Catal. Commun.* **2013**, *40*, 1–4. [CrossRef]
46. Anandan, S.; Rao, T.N.; Gopalan, R.; Ikuma, Y. Fabrication of visible-light-driven N-doped ordered mesoporous TiO_2 photocatalysts and their photocatalytic applications. *J. Nanosci. Nanotechnol.* **2014**, *14*, 3181–3186. [CrossRef]
47. Zou, Z.G.; Ye, J.H.; Arakawa, H. Photocatalytic behavior of a new series of $In_{0.8}M_{0.2}TaO_4$ (M = Ni, Cu, Fe) photocatalysts in aqueous solutions. *Catal. Lett.* **2001**, *75*, 209–213. [CrossRef]
48. Luan, J.F.; Li, M.; Ma, K.; Li, Y.M.; Zou, Z.G. Photocatalytic activity of novel Y_2InSbO_7 and Y_2GdSbO_7 nanocatalysts for degradation of environmental pollutant rhodamine B under visible light irradiation. *Chem. Eng. J.* **2011**, *167*, 162–171. [CrossRef]
49. Luan, J.F.; Ma, K.; Pan, B.C.; Li, Y.M.; Wu, X.S.; Zou, Z.G. Synthesis and catalytic activity of new Gd_2BiSbO_7 and Gd_2YSbO_7 nanocatalysts. *J. Mol. Catal. A-Chem.* **2010**, *321*, 1–9. [CrossRef]
50. Eder, D.; Motta, M.; Windle, A.H. Iron-doped Pt-TiO_2 nanotubes for photo-catalytic water splitting. *Nanotechnology* **2009**, *20*, 055602. [CrossRef]
51. Biswas, S.K.; Baeg, J.O. Enhanced photoactivity of visible light responsive W incorporated $FeVO_4$ photoanode for solar water splitting. *Int. J. Hydrog. Energy* **2013**, *38*, 14451–14457. [CrossRef]
52. Xu, X.L.; Song, W. Synthesis and photocatalytic activity of heterojunction $ZnFe_2O_4$-$BiVO_4$. *Mater. Technol.* **2017**, *32*, 472–479. [CrossRef]
53. Zong, X.; Yan, H.J.; Wu, G.P.; Ma, G.J.; Wen, F.Y.; Wang, L.; Li, C. Enhancement of photocatalytic H_2 evolution on CdS by loading MOS_2 as cocatalyst under visible light irradiation. *J. Am. Chem. Soc.* **2008**, *130*, 7176–7177. [CrossRef]
54. Zong, X.; Han, J.F.; Ma, G.J.; Yan, H.J.; Wu, G.P.; Li, C. Photocatalytic H_2 evolution on CdS loaded with WS_2 as cocatalyst under visible light irradiation. *J. Phys. Chem. C* **2011**, *115*, 12202–12208. [CrossRef]
55. Chen, X.F.; Zhang, J.; Huo, Y.N.; Li, H.X. Preparation and visible light catalytic activity of three-dimensional ordered macroporous CdS/TiO_2 fifilms. *Chin. J. Catal.* **2013**, *34*, 949–955. [CrossRef]
56. Pirhashemi, M.; Habibi-Yangjeh, A. Photosensitization of ZnO by AgBr and Ag_2CO_3: Nanocomposites with tandem n-n heterojunctions and highly enhanced visible-light photocatalytic activity. *J. Colloid Interface Sci.* **2016**, *474*, 103–113. [CrossRef]
57. Cao, J.; Xu, B.Y.; Lin, H.L.; Luo, B.D.; Chen, S.F. Novel Bi_2S_3 -sensitized BiOCl with highly visible light photocatalytic activity for the removal of rhodamine B. *Catal. Commun.* **2012**, *26*, 204–208. [CrossRef]
58. Lu, H.J.; Xu, L.L.; Wei, B.; Zhang, M.Y.; Gao, H.; Sun, W.J. Enhanced photosensitization process induced by the p-n junction of $Bi_2O_2CO_3$/BiOCl heterojunctions on the degradation of rhodamine B. *Appl. Surf. Sci.* **2014**, *303*, 360–366. [CrossRef]
59. Biswas, S.; Sundstrom, V.; De, S. Facile synthesis of luminescent TiO_2 nanorods using an anionic surfactant: Their photosensitization and photocatalytic effificiency. *Mater. Chem. Phys.* **2014**, *147*, 761–771. [CrossRef]
60. Han, C.C.; Ge, L.; Chen, C.F.; Li, Y.J.; Xiao, X.L.; Zhang, Y.N.; Guo, L.L. Novel visible light induced Co_3O_4 -g-C_3N_4 heterojunction photocatalysts for effificient degradation of methyl orange. *Appl. Catal. B Environ.* **2014**, *147*, 546–553. [CrossRef]
61. Xie, T.P.; Liu, C.L.; Xu, L.J.; Yang, J.; Zhou, W. Novel heterojunction Bi_2O_3/$SrFe_{12}O_{19}$ magnetic photocatalyst with highly enhanced photocatalytic activity. *J. Phys. Chem. C* **2013**, *117*, 24601–24610. [CrossRef]
62. Dai, K.; Lv, J.L.; Lu, L.H.; Liang, C.H.; Geng, L.; Zhu, G.P. A facile fabrication of plasmonic g-C_3N_4/Ag_2WO_4/Ag ternary heterojunction visible-light photocatalyst. *Mater. Chem. Phys.* **2016**, *177*, 529–537. [CrossRef]
63. Wang, X.F.; Hu, H.M.; Chen, S.H.; Zhang, K.H.; Zhang, J.; Zou, W.S.; Wang, R.X. One-step fabrication of BiOCl/CuS heterojunction photocatalysts with enhanced visible-light responsive activity. *Mater. Chem. Phys.* **2015**, *158*, 67–73. [CrossRef]
64. Luan, J.F.; Wang, S.; Ma, K.; Li, Y.M.; Pan, B.C. Structural Property and Catalytic Activity of New In_2YbSbO_7 and Gd_2YbSbO_7 Nanocatalysts under Visible Light Irradiation. *J. Phys. Chem. C.* **2010**, *114*, 9398–9407. [CrossRef]
65. Sun, S.F.; Wu, Y.F.; Zhang, X.; Zhang, Z.J.; Yan, Y.; Guan, W.S. Enhanced visible-light-driven photocatalytic degradation performance of cip on $BiVO_4$-Bi_2WO_6 nano-heterojunction photocatalysts. *Nona* **2014**, *9*, 1450015. [CrossRef]
66. Yang, B.Y.; Li, H.; Shang, N.Z.; Feng, C.; Gao, S.T.; Wang, C. Visible-Light Responsive Photocatalyst g-C_3N_4@BiOCl with Hollow Flower-like Structure: Preparation and Photocatalytic Performance. *Chin. J. Inorg. Chem.* **2017**, *33*, 396–404.
67. Nguyen, T.B.; Doong, R.A. Heterostructured $ZnFe_2O_4$/TiO_2 nanocomposites with a highly recyclable visible-light-response for bisphenol A degradation. *RSC Adv.* **2017**, *7*, 50006–50016. [CrossRef]

68. Simsek, E.B.; Kilic, B.; Asgin, M.; Akan, A. Graphene oxide based heterojunction TiO_2-ZnO catalysts with outstanding photocatalytic performance for bisphenol-A, ibuprofen and flurbiprofen. *J. Ind. Eng. Chem.* **2018**, *59*, 115–126. [CrossRef]
69. Zhang, C.J.; Li, N.J.; Chen, D.Y.; Xu, Q.F.; Li, H.; He, J.H.; Lu, J.M. The ultrasonic-induced-piezoelectric enhanced photocatalytic performance of ZnO/CdS nanofibers for degradation of bisphenol A. *J. Alloy. Compd.* **2021**, *885*, 160987. [CrossRef]
70. Luo, Y.D.; Wei, X.Q.; Gao, B.; Zou, W.X.; Zheng, Y.L.; Yang, Y.C.; Zhang, Y.; Tong, Q.; Dong, L. Synergistic adsorption-photocatalysis processes of graphitic carbon nitrate (g-C_3N_4) for contaminant removal: Kinetics, models, and mechanisms. *Chem. Eng. J.* **2019**, *375*, 122019. [CrossRef]
71. Vo, T.S.; Vo, T.T.B.C.; Suk, J.W.; Kim, K. Recycling performance of graphene oxide-chitosan hybrid hydrogels for removal of cationic and anionic dyes. *Nano Converg.* **2020**, *7*, 4. [CrossRef]
72. Zyoud, A.H.; Saleh, F.; Helal, M.H.; Shawahna, R.; Hilal, H.S. Anthocyanin-Sensitized TiO_2 Nanoparticles for Phenazopyridine Photodegradation under Solar Simulated Light. *J. Nanomater.* **2018**, *2018*, 2789616. [CrossRef]
73. Kohantorabi, M.; Moussavi, G.; Oulego, P.; Giannakis, S. Heterogeneous catalytic ozonation and peroxone-mediated removal of Acetaminophen using natural and modified hematite-rich soil, as efficient and environmentally friendly catalysts. *Appl. Catal. B-Environ.* **2022**, *301*, 120786. [CrossRef]
74. Rostami, R.; Moussavi, G.; Darbari, S.; Jafari, A.J. Non-thermal plasma by positive corona glow discharge using nano-structured Cu/CuO coated electrodes for benzene removal from air flow; removal enhancement and energy efficiency improvement. *Sep. Purif. Technol.* **2021**, *275*, 119156. [CrossRef]
75. Kohantorabi, M.; Moussavi, G.; Mohammadi, S.; Oulego, P.; Giannakis, S. Photocatalytic activation of peroxymonosulfate (PMS) by novel mesoporous Ag/ZnO@$NiFe_2O_4$ nanorods, inducing radical-mediated acetaminophen degradation under UVA irradiation. *Chemosphere* **2021**, *277*, 130271. [CrossRef]
76. Kohantorabi, M.; Moussavi, G.; Oulego, P.; Giannakis, S. Radical-based degradation of sulfamethoxazole via UVA/PMS-assisted photocatalysis, driven by magnetically separable Fe_3O_4@CeO_2@BiOI nanospheres. *Sep. Purif. Technol.* **2021**, *267*, 118665. [CrossRef]
77. Khavar, A.H.C.; Moussavi, G.; Mahjoub, A.R.; Satari, M.; Abdolmaleki, P. Synthesis and visible-light photocatalytic activity of In, S-TiO_2@rGO nanocomposite for degradation and detoxification of pesticide atrazine in water. *Chem. Eng. J.* **2018**, *345*, 300–311. [CrossRef]
78. Namini, A.S.; Delbari, S.A.; Mousavi, M.; Ghasemi, J.B. Synthesis and characterization of novel ZnO/$NiCr_2O_4$ nanocomposite for water purification by degradation of tetracycline and phenol under visible light irradiation. *Mater. Res. Bull.* **2021**, *139*, 111247. [CrossRef]
79. Nguyen, V.H.; Mousavi, M.; Ghasemi, J.B.; Delbari, S.A.; Le, Q.V.; Asl, M.S.; Shokouhimehr, M.; Mohammadi, M.; Azizian-Kalandaragh, Y.; Namini, A.S. Synthesis, characterization, and photocatalytic performance of Ag/$AgFeO_2$ decorated on g-C3N4-nanosheet under the visible light irradiation. *J. Taiwan Inst. Chem. Eng.* **2020**, *115*, 279–292. [CrossRef]
80. Nguyen, V.H.; Mousavi, M.; Ghasemi, J.B.; Delbari, S.A.; Le, Q.V.; Namini, A.S.; Asl, M.S.; Shokouhimehr, M.; Azizian-Kalandaragh, Y.; Mohammadi, M. Z-scheme g-C_3N_4 nanosheet/$MgBi_2O_6$ systems with the visible light response for impressive photocatalytic organic contaminants degradation. *J. Photoch. Photobio. A.* **2021**, *406*, 113023. [CrossRef]
81. Nguyen, V.H.; Mousavi, M.; Ghasemi, J.B.; Le, Q.V.; Delbari, S.A.; Asl, M.S.; Shokouhimehr, M.; Mohammadi, M.; Azizian-Kalandaragh, Y.; Namini, A.S. In situ preparation of g-C_3N_4 nanosheet/FeOCl: Achievement and promoted photocatalytic nitrogen fixation activity. *J. Colloid. Interf. Sci.* **2021**, *587*, 538–549. [CrossRef]
82. Nguyen, V.H.; Mousavi, M.; Ghasemi, J.B.; Le, Q.V.; Delbari, S.A.; Namini, A.S.; Asl, M.S.; Shokouhimehr, M.; Jang, H.W.; Mohammadi, M. 8g-C_3N_4 nanosheet adorned with Ag_3BiO_3 as a perovskite: An effective photocatalyst for efficient visible-light photocatalytic processes. *Mater. Sci. Semicon. Proc.* **2021**, *125*, 105651. [CrossRef]
83. Wang, J.H.; Zou, Z.G.; Ye, J.H. Synthesis, Structure and Photocatalytic Property of a New Hydrogen Evolving Photocatalyst Bi_2InTaO_7. *Mater. Sci. Forum.* **2003**, *423–425*, 485–490. [CrossRef]
84. Kohno, M.; Ogura, S.; Sato, K.; Inoue, Y. Properties of photocatalysts with tunnel structures: Formation of a surface lattice O− radical by the UV irradiation of $BaTi_4O_9$ with a pentagonal-prism tunnel structure. *Chem. Phys. Lett.* **1997**, *267*, 72–76. [CrossRef]
85. Kudo, A.; Kato, H.; Nakagawa, S. Water Splitting into H_2 and O_2 on New $Sr_2M_2O_7$ (M = Nb and Ta) Photocatalysts with Layered Perovskite Structures: Factors Affecting the Photocatalytic Activity. *J. Phys. Chem. B* **2000**, *104*, 571–575. [CrossRef]
86. Nowak, M.; Kauch, B.; Szperlich, P. Determination of energy band gap of nanocrystalline SbSI. *Rev. Sci. Instrum.* **2009**, *80*, 046107. [CrossRef]
87. Zhou, F.; Kang, K.; Maxisch, T.; Ceder, G.; Morgan, D. The electronic structure and band gap of $LiFePO_4$ and $LiMnPO_4$. *Solid State Commun.* **2004**, *132*, 181–186. [CrossRef]
88. Tauc, J.; Grigorov, R.; Vancu, A. Optical properties and electronic structure of amorphous germanium. *Phys. Status Solidi* **1966**, *15*, 627–637. [CrossRef]
89. Butler, M.A. Photoelectrolysis with $YFeO_3$ electrodes. *J. Appl. Phys.* **1977**, *48*, 1914–1920. [CrossRef]
90. Cui, B.Y.; Cui, H.T.; Li, Z.R.; Dong, H.Y.; Li, X.; Zhao, L.F.; Wang, J.W. Novel $Bi_3O_5I_2$ hollow microsphere and its enhanced photocatalytic activity. *Catalysts* **2019**, *9*, 709. [CrossRef]
91. Vallejo, W.; Cantillo, A.; Salazar, B.; Diaz-Uribe, C.; Ramos, W.; Romero, E.; Hurtado, M. Comparative study of ZnO thin films doped with transition metals (Cu and Co) for methylene blue photodegradation under visible irradiation. *Catalysts* **2020**, *10*, 528. [CrossRef]

92. Deonikar, V.G.; Patil, S.S.; Tamboli, M.S.; Ambekar, J.D.; Kulkarni, M.V.; Panmand, R.P.; Umarji, G.G.; Shinde, M.D.; Rane, S.B.; Munirathnam, N.R.; et al. Growth study of hierarchical $Ag_3PO_4/LaCO_3OH$ heterostructures. *Phys. Chem. Chem. Phys.* **2017**, *19*, 20541–20550. [CrossRef] [PubMed]
93. Patil, S.S.; Tamboli, M.S.; Deonikar, V.G.; Umarji, G.G.; Ambekar, J.D.; Kulkarni, M.V.; Kolekar, S.S.; Kale, B.B.; Patil, D.R. Magnetically separable $Ag_3PO_4/NiFe_2O_4$ composites with enhanced photocatalytic activity. *Dalton Trans.* **2015**, *44*, 20426–20434. [CrossRef] [PubMed]
94. Jiang, L.B.; Yuan, X.Z.; Zeng, G.M.; Liang, J.; Chen, X.H.; Yu, H.B.; Wang, H.; Wu, Z.B.; Zhang, J.; Xiong, T. In-situ synthesis of direct solid-state dual Z-scheme $WO_3/g\text{-}C_3N_4/Bi_2O_3$ photocatalyst for the degradation of refractory pollutant. *Appl. Catal. B* **2018**, *227*, 376–385. [CrossRef]
95. Cao, W.; Jiang, C.Y.; Chen, C.; Zhou, H.F.; Wang, Y.P. A novel Z-scheme $CdS/Bi_4O_5Br_2$ heterostructure with mechanism analysis: Enhanced photocatalytic performance. *J. Alloys Compd.* **2021**, *861*, 158554. [CrossRef]